Australian Institute of Nuclear Science and Engineering

15th Australian Conference on Nuclear and Complementary Techniques of Analysis & 9th Vacuum Society of Australia Congress

The University of Melbourne
21st - 23rd November 2007

PROCEEDINGS

Australian Government
Australian Research Council

ThermoFisher
SCIENTIFIC
The world leader in serving science

AP Instruments Pty Ltd

Andre Peters ***33 Hunter Ave St Ives 2075 NSW***
02 91446600 0448 750 885 andrepeters@optusnet.com.au

PREVAC *www.prevac.eu*

- Ultra High Vacuum and High Vacuum System
- Manipulators, Goniometers and Mechanical Feedthroughs
- Chambers and Mechanisms
- Sample Holders
- X-Ray , Electron, Ion sources
- **Accessories**
  Bakeout equipment, Load locks, Vacuum doors, Mass flow controllers, Water cooling devices, vacuum fittings, Titanium sublimation pumps etc.
- Eelectronics

Pressure measurements, Stepping motors controls, Emission regulators, Electron beam evaporator PS, Electron and Ion source PS, Bakeout control units. etc

- Software

TOF acquisition applications, Space simulator control appl. , Dedicated software for Customer's systems and devices, Pressure control appl. , Thermal desorption Spectroscopy Control, Automatisation of sample transfers, etc.

TOYAMA www.toyama-jp.com

Synchrotron Radiation (SR) Beam Line and Related Systems

Total Beam Line Systems
Branch Beam Shutters
Absorbers
Mirror Positioning Systems(3-7 axes,Bent type)
Monochromators(VUV,Soft X-ray,Photoelectron)
Analysis Instruments
Beam Monitors
Beam Ducts
Slits
Pumping Units for Vacuums

Particle Accelerators and Related Devices

Magnets(Bending,Quadrupole,Multipole,Steering,etc.)
Monitors(Profile Monitors,Core Monitors,Current Monitors,etc.)
Ion Sources
Electron Guns
Infectors,Deflectors
Accelerating Electrodes
Beam Ducts
Pumping Units for Vacuums
Analyzers

Other Systems and Components

Experiment Systems and Instruments for Space Development,
Condensed Matter Physics and Electrical Engineerings

Systems and Instruments for Nuclear Fusion and Nuclear Engineering

Ion Source Drawing Electrodes
Calibration Spectroscopes for Plasma
Measuring Instruments
High-Frequency Antennas for Plasma Heating
Beam Dumps
Fixed/Movable Limiters
Calorimeters
Collimators
Manipulator Tongs

Vacuum Experiment Systems and Instruments

Vacuum Chambers(Low to Ultra-High Vacuum(LV-UHV) in various configurations for all types of applications)
Instruments for Plasma Experiments
Pumping Units for Vacuums

Various Parts & Components for Vacuum Experiments

Fittings
Feed Throughs
Linear/Rotary Motion Drivers,Linear Motion Thimbles
Magnet Couplings,Manipulators
Current Conductors,Electrical Isolators;
Goniometers

Program
Tuesday 20th November 2007

16:30 - 18:30	Registration
17:30 - 19:30	Welcome and light refreshments

Wednesday 21st November 2007

		Page
08:15 - 09:15	Registration	
09:15 - 09:40	Welcome	
Session 1	**Environment and Bioscience (1)** **Chair: Jeff McCallum**	
09:40 -10:20	David Paterson, Australian Synchrotron Microanalysis capabilities of the microspectroscopy beamline at the Australian Synchrotron	15
10:20 - 10:40	Samuel Marx, University of Queensland Evidence of enhanced El Niño activity in the mid Holocene inferred from records of Australian dust deposition in New Zealand.	17
10:40 - 11:00	Dora Pearce, University of Ballarat Toenails: they know where you've been!	21
11:00 - 11:30	Morning Tea	
Session 2	**Advanced Materials and Analysis** **Chair: Rob Elliman**	
11:30 - 12:00	Daniel Riley, University of Melbourne Use of ultra-fast diffraction in the design of novel materials	27
12:00 - 12:20	Imam Kambali, University of Newcastle Determination of hydrogen adsorption site on palladium(100) using low energy ion scattering spectroscopy	33
12:20 - 12:40	Babs Fairchild, University of Melbourne Fabrication of sub micron layers in single-crystal diamond	36
12:40 - 13:10	Claudia Schnohr, Australian National University Comparison of the atomic structure in InP amorphised by electronic or nuclear ion-energy-loss processes	37
13:10 - 14:30	Lunch	
Session 3	**Environment, Bioscience (2) and Nanotechnology (1)** **Chair: Peter Johnston**	
14:30 - 15:00	Paul Pigram, Latrobe University Detecting oligonucleotide immobilization and hybridisation using TOF-SIMS	42
15:00 - 15:20	Robert Haworth, University of New England Blending lead-210 and AMS age profiles from estuarine sediment cores to reconstruct Holocene climate change in the Sydney Region	43

15:20 - 15:40	Andreas Markwitz, GNS Low energy lead implantation into Si for novel group IV nanomaterials	46
15:40 - 16:00	Michael Gladys, University of Newcastle Bridging the gap between the nano-particle and single crystal surface science	50
16:00 - 16:30	Paul Munroe, University of NSW Application of focused ion beam systems to materials analysis	53
16.30 – 18.30	**Poster Session 1** and Afternoon Tea	
18:00 onwards	BBQ	

Thursday 22nd November 2007

Session 4	**Environment and Bioscience (3)** **Chair: David Cohen**	
09:00 - 09:30	James Robertson, AFP Nuclear science and forensic science - complementary sciences!	57
09:30 - 09:50	Serena Abbondante, University of Canberra Radiologically contaminated evidence: extraction procedures and the effect of radioactive materials on forensic DNA profiling	58
09:50 - 10:10	Laura Gladkis, ADFA@UNSW A new methodology in prosthesis research: radioisotope tracing of knee implant wear	60
10:10 - 10:30	Amy Ziebell, University of Wollongong Cylindrical silicon-on-insulator microdosimeter: charge collection characteristics	65
10:30 - 11:00	Julian Adams, Australian Synchrotron Protein crystallography using the Australian Synchrotron	68
11:00 - 11:30	Morning Tea	
Session 5	**Nanotechnology (2)** **Chair: Andreas Markwitz**	
11:30 - 12:00	Matt Kilburn, University of Western Australia NanoSIMS: Recent advances and new applications in SIMS	68
12:00 - 12:20	Damian Carder, GNS Ion-beam sputtered germanium thin films – self-assembly of surface nanostructure using post growth annealing	769
12:20 - 12:40	Michael Dunn, University of Melbourne Interface trap density reduction in thin silicon oxides using ion Implantation	73
12:40 - 13:00	Dinesh Venkatachalam, RMIT Surface fraction statistics of gold nanoclusters of dissimilar sizes determined by RBS	77

13:00 - 13:30	Rob Elliman, Australian National University Photonic nanostructures and their influence on Er luminescence	81
13:30 - 14:30	Lunch	
14:30 – 18:30	**Conference Tour of Synchrotron**	
19:00 - 22:30	**Conference Dinner at Treetops Restaurant, Melbourne Museum**	

Friday 23rd November 2007

09:00	**Session 6: Advanced Materials, Devices and Analysis Chair: Chris Ryan**	
09:00 - 09:30	John Kennedy, GNS Unravelling the mystery of zinc oxide	85
09:30 - 09:50	Julius Orwa, University of Melbourne Towards a formula for optimized production of single NV centres in diamond by ion implantation	89
09:50 - 10:10	Kane O'Donnell, University of Newcastle Neutral atom microscopy: a non-destructive, high-resolution surface analysis technique	89
10:10 - 10:30	Andrew Baloglow, University of Wollongong Characterization of silicon detectors utilized in an on-line dosimetry system for microbeam radiation therapy	90
10:30 - 10:50	Perry Davy, GNS Diffusion characteristics of silicon implanted with group IV elements	94
10:50 - 11:20	Rachel Caruso, University of Melbourne Porous titanium dioxide materials fabricated by using templating techniques	97
11:10 - 11:30	Morning Tea	
11:30 -13:00	**Poster Session 2**	
13:00 - 14:00	Lunch	
14:00 - 16:30	**Session 7: Ion Beam Science and Advances in Analysis Chair: David Jamieson**	
14:00 - 14:30	John O'Connor, University of Newcastle Helium ion microscope – high resolution, high contrast microscopy for nanotechnology	99

14:30 - 14:50	Chris Ryan, CSIRO Next generation x-ray microspectroscopy: towards full-spectral XANES and high throughput fluorescence imaging using massively parallel detector arrays and realtime spectral deconvolution	100
14:50 - 15:10	Michael Went, Australian National University Extended interface analysis using high energy electron scattering	104
15:10 - 15:30	Changyi Yang, University of Melbourne Avalanche detector technology for keV single ion detection and implantation for quantum bits construction	108
15:30 - 15:50	David Cohen, ANSTO Towards a better understanding and prediction of the bremsstrahlung background in PIXE spectra	111
15:50 – 16:10	Andrew Gleadow, University of Melbourne Fully-automated counting of fission tracks in natural minerals for fission track dating and thermochronology	116
16:10 - 16:40	David Belton, CSIRO PIXE imaging of a developing corrosion front beneath a protective coating on galvanized steel	119

16:40 - 17:00 Closing Remarks and Award of Prizes

Posters index

N. Biluš Abaffy	Deposition of high quality metal oxide thin films using a filtered cathodic vacuum arc	124
A. Alves	Detection and placement of single ions in the keV and MeV regimes: MeV ion-aperture scattering	127
K. Belay	The effect of annealing temperature on the optical properties of sputter-deposited hafnium oxide thin films	133
John W. Bennett	The introduction of the k0-method of neutron activation analysis at ANSTO	136
M. Bhaskaran	Investigation of surface crystallites on C54 titanium silicide thin films using transmission electron microscopy	140
Jaroslav Blazek	Structural parameters of wheat starch granules differing in amylose content and functional characteristics studied by small-angle x-ray scattering	143
D. Button	The ANSTO ECR ion source and its application to mass spectrometry	147
M. R. J. Carroll	Design considerations in the development of magnetic nanoparticles for MRI contrast enhancement	152
C. Chaiwong	Plasma immersion ion implantation and deposition of titanium nitride onto polymers	153
C. T. Chang	DLTS study of ion and molecular implantation damage in silicon	157
Martin A. Cole	Surface modifications of nanoporous alumina membranes by plasma polymerisation	161
Gavin Conibeer	Characterisation of nanostructures for photovoltaics	166
M. A. Draganski	The refractive index of ion implanted diamond	167
Glenna L. Drisko	Metal oxides produced from sol-gel templating of agarose gel applied to vanadium adsorption	168
Daniel W. Drumm	Optimisation of Density Functional Theory (DFT) parameters for calculating the electronic and optical properties of diamond.	170
Barbara Etschmann	XANES from ROI vs. DA deconvolution of full spectral SXRF data	175
Jing-Hua Fang	Fabrication of periodic Al_2O_3 nanomasks	179
Fang Fang	High temperature electronic properties of field-effect transistor based on SiC nanowires	182
V.S. Gill	Age mapping of radioisotopes by daughter trace element analysis	185
M. J. Gladys	Enantioselectivity of chiral molecules on chiral copper surfaces	189
Sarah K. Hagerty	Delineating groundwater flowpaths using ^{14}C dating in the Upper Loddon catchment, central Victoria	195
M. Ionescu	ANSTO heavy ion ToF for analysis of light elements in thin films	196

B. C. Johnson	Dopant enhanced hydrogen diffusion in amorphous silicon layers	202
M Hult	On the use of mercury as a means of locating background sources in ultra low background HPGe-detector systems	206
L. M. Jong	Identification of ion strike location by precision IBIC	207
Anthony G Kachenko	Nuclear microprobe studies of metal(loid)s distribution in hyperaccumulating plants	211
Teera Kamvong	PIXE/PIGE microanalysis of trace elements in hydrothermal magnetite and exploration significance: a pilot study	216
John V Kennedy	Transmission electron microscopy studies of polycrystalline zinc oxide thin films grown by ion beam sputtering	220
Taehyun Kim	The synthesis and structure of silica nanowires	224
Bruce V. King	SIMS and SNMS analysis of solar wind implanted silicon from the NASA Genesis Mission	228
Bao-ping Li	Differentiation of white-bodied ancient ceramics from north China kilns: the ICP-MS and TIMS techniques and their significance	229
Anwaar Malik	Carbon cluster output from SNICS: Impact angle dependence	233
Zeya Oo	*In-Situ* study of the self-recovery property in aluminium titanate	233
Manickam Minakshi	Examining Manganese Dioxide as a cathode in aqueous LiOH battery	234
Patrick T Moss	Comparative ages of pollen and foraminifera in the ODP 820 marine core	241
Anthony Musumeci	Application of radioisotopes for nanotoxicological studies	245
Ashley Natt	Preliminary paleolimnological data from a Santiago Island coastal lagoon, Galapagos Archipelago, Ecuador	249
Huynh Nguyen	Mechanical properties of cortical bone allografts irradiated at a series of gamma doses from 5 to 25 kGy	250
R. Nigam	Superconducting and magnetic properties of $RuSr_2$ $(Eu_{1.5}Ce_{0.5})Cu_2O_{10}$	254
G. J. Oberman	Drying of a sol gel droplet suspended in a flowing atmosphere	258
D. J. O'Connor	Surface structure analysis of Ni/Cu(100), Fe/Cu(100) and Ni/Fe/Cu(100)	262
D. J. O'Connor	Helium ion microscope - high resolution, high contrast microscopy for nanotechnology	262
W. K. Pang	Depth-profiling of thermal dissociation of Ti_3SiC_2 in vacuum	263
J. G. Partridge	Deposition of high quality metal and metal oxide thin films using a filtered cathodic vacuum arc	267

J.R. Prescott	Thermoluminescence spectra of quartz from single crystals	268
Daniel Pyke	Raman measurements of hydrogen ions implanted into silicon	272
Daniel Pyke	Hydrogen refinement during solid phase epitaxial crystallisation of buried amorphous silicon layers	276
M. Raiber	Application of environmental isotopes to study aquifer interactions and their impact on groundwater salinisation in western Victoria	282
A.B.Rosenfeld	Investigation of monolithic Si ΔE-E telescope using IBIC and application for radiobiological efficiency estimation in proton therapy	283
Y M Sabri	Gold nano-structures electroplated on au electrodes of quartz crystal microbalance (QCM) for enhanced mercury vapour sensitivity	287
R. Siegele	Localisation of trace metals in hyper-accumulating plants using μ-PIXE	292
Vijay Sivan	Wafer scale etching of lithium niobate using conventional diffusion process	296
Michael Smith	Establishment of efficiency function for the gamma-ray spectrometry system	296
Paul Spizzirri	A TEM study of Si-SiO_2 interfaces in silicon nanodevices	297
Paul Spizzirri	Characterisation of high quality, thermally grown silicon dioxide on silicon	301
Paul Spizzirri	An EPR study on the activation of low energy phosphorus ions implanted into silicon	305
S. Sriram	Modified unit cell of preferentially oriented strontium-doped lead zirconate titanate thin films on Pt/TiO_2/Si	310
Alexander M. St John	Separation of uranium using polymer inclusion membranes	314
Eduard Stelcer	Ion beam analysis and positive matrix factorisation modeling: tools for exploring aerosol source fingerprints	318
Jessica A. van Donkelaar	Single ion implantation using nano-apertures: precision placement for CTAP	322
L. Velleman	Template fabricated gold nanotubes membranes: a nucleation and growth study	326
Dinesh Kumar Venkatachalam	Surface fraction statistics of gold nanoclusters of dissimilar sizes determined by RBS	330
Byron J. Villis	A low energy, angle dependent, defect study of H implanted Si	334
Xingdong Wang	Synthesis, characterization and photocatalytic application of porous Au/TiO_2 nano-hybrids	338
J.L. Wang	Magnetic phase transitions in $PrMn_{2-x}Fe_xGe_2$	342
Mark Thomas Warne	History of natural environmental events in a pristine estuary: ostracod proxies and ^{210}Pb chronology from Wingan Inlet, Victoria	344
A-M. M. Williams	Iron deposition in archaeological teeth	348

Myint Zaw	Oxidation profiles of arsenic, iron, manganese and uranium in tailings dam samples using x-ray absorption near-edge structure spectroscopy	352
Waven Zhang	Reduction of titanium dioxide: comparison of analysis by Raman spectroscopy and XRD	358
B. Zorko	Measurement of actinides by the unfocused beam AMS	363

Application of radioisotopes for nanotoxicological studies

Anthony Musumeci [1,2], Suzanne Smith [3], Gordon Xu [1,2] and Darren Martin [1,2]

[1.] *Australian Institute of Bioengineering and Nanotechnology, The University of Queensland, Brisbane QLD 4072, Australia.*

[2.] *ARC Centre of Excellence for Functional Nanomaterials, School of Engineering, The University of Queensland, Brisbane QLD 4072, Australia.*

[3.] *Centre of Excellence for Antimatter-Matter Studies, Australian Nuclear Science and Technology Organisation, Menai, NSW 2234, Australia.*

a.musumeci@uq.edu.au

Introduction

The impact of nanotechnology on a broad range of industry sectors continues to grow at an unprecedented rate, with the National Science Foundation expecting nanotechnology to play a part in a trillion dollar industry by 2015. The potential benefits of nanotechnology for industries from new advanced materials, to biotechnology, quantum computing, energy and the environment, and the community in general, has been highlighted in numerous publications [1-3]. Unfortunately, these new nanomaterials, nanoparticles and nanotechnologies are appearing faster than our capacity to fully-evaluate their potential impact on health, the environment and safety.

Consequently, the sustainability of this industry may be dependent on understanding and managing the unwanted effects that nanoparticles and nanostructured materials may have on the environment and human health, both in the short term and long term.

Nanoparticles have been present in the environment throughout evolution. However, many of the novel engineered structures that are being developed for industry use have unique structures, shapes, functionality and chemical compositions. It is now established that particles of the same chemical composition but of different size and shape can have markedly different biological responses [4]. Many of the traditional approaches used to assess particle toxicology do not apply to nanoscale particles because of their unique interactions with cells and tissues [5]. Moreover, significant challenges arise in detecting and monitoring very small particles in the environment.

Radiolabelling of nanoparticles is one such technique that has the ability to offer high sensitivity and the incorporation of only nano to pico molar concentrations of radiotracer probes for non-invasive imaging by single photon emission computed tomography or positron emission tomography. Such radiotracer techniques are also inherently rapid and are not affected by strong media or electrolyte solutions. Radiotracer probes also offer a range in half-life (from hours to days) and emission profile (gamma and/or positron emitting) depending on the length of *in vivo* or *in vitro* study desired. Finally, detection of the radiotracer can be achieved with minimal handling which provides for greater accuracy.

A number of recent studies have provided a growing indication that nanoparticles can exert adverse effects upon biological systems [2, 3, 6]. Despite these disturbing findings, none of these studies report a complete and extensive characterisation of the nanoparticles in question which are instrumental to understanding the systemic biological and physicochemical characteristics observed.

Thus, what is missing in scientific literature is a study of the toxicology of well characterised nanoparticles. Currently, the absence of such robust, quality safety assessments for new technologies are already beginning to produce a negative consumer reaction that could result in adverse outcomes for the whole of the industry

not unlike that experienced by the genetically modified foods industry [7]. Proactive education and communication with the public based on quality research is vital and required promptly to avoid similar misconceptions. This paper provides an initial report to the feasibility of radioisotopes as labels for a series of well characterised layered double hydroxide (LDH) nanoparticles.

Method and Materials

LDHs are a class of anionic clay that can be synthesised in the laboratory with specific spatial characteristics. Structurally, LDHs consist of brucite-like hydroxide layers ($Mg(OH)_2$) with some isomorphous substitution by trivalent cations which give rise to a net positive surface charge. To be able to track these nanoparticles *in vitro* and *in vivo*, isomorphous substitution of radio-emitting species (*i.e.* ^{57}Co and ^{67}Ga) into the octahedral brucite-like layer during LDH crystallisation is undertaken. To balance the positively charged layers, various anions (*i.e.* CO_3, Cl, SO_4) as well as water are present in the interlayer cavity (see Fig 1).

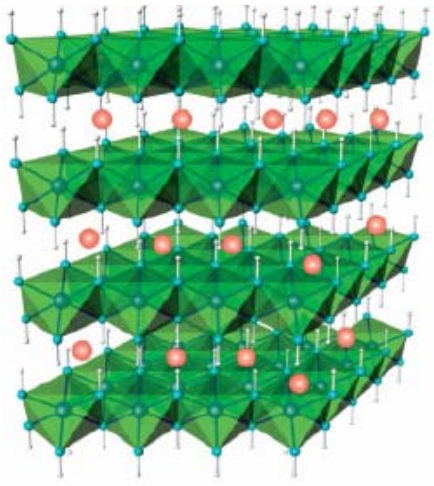

Figure 1: Schematic crystal structure of LDH showing positively charged brucite-like octahedral layers counterbalanced by interlayer anions [8]

LDH nanoparticles of the chemical formula $Mg_2Al(OH)_6(CO_3)_{0.5}.2H_2O$ were synthesised using a similar methodology outlined by Xu *et al*. [11]. In brief, 10mL of a mixed metal salt solution containing $MgCl_2$ (2.0mmol), $AlCl_3$ (1.0mmol) and a small volume of $^{57}CoCl_2$ (10^{-9} – 10^{-12} M, with a known level of activity) was quickly added (within 5sec) into 40mL of a base solution containing NaOH (6.0mmol) and Na_2CO_3 (0.6mmol) under vigorous stirring.The LDH slurry was subject to centrifugation and washed twice with H_2O and then redispersed in 40mL of H_2O via vigorous shaking. (Note: all water used in experiments was milli-Q H_2O (18.2 MΩ)). The aqueous dispersion was then transferred into a teflon lined stainless steel autoclave (45mL) and placed into a preheated 100°C oven for 4 hours. After air-cooling (for at least 3 hours) following hydrothermal treatment, a stable and homogenous LDH suspension resulted. Characterisation of the nanoparticles was undertaken using a combination of thin layer chromatography (TLC), X-ray diffraction (XRD), dynamic light scattering (DLS) and transmission electron microscopy (TEM).

Results and Discussion

In general the as-synthesised ^{57}Co intercalated LDH nanoparticles were found to have an average hydrodynamic particle size of 68nm from DLS measurements. TEM images confirmed the presence of well dispersed hexagonal platelets in solution, with minimal amorphous content and impurities. Additionally, the nanoparticles formed a single crystalline LDH phase with interlayer spacing (d_{003}) of 7.6 Å, as determined from XRD (Fig. 2).

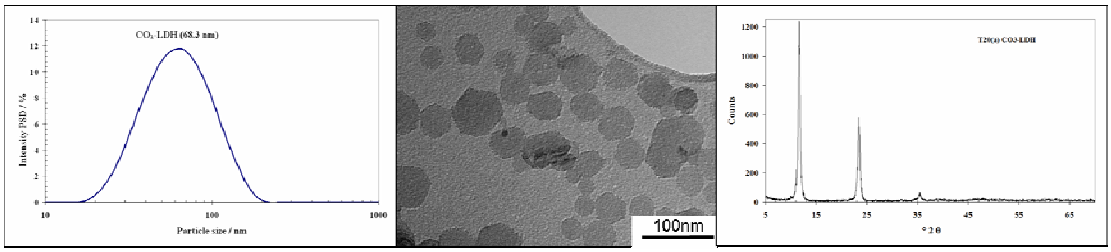

Figure2(a) DLS plot of intensity derived mean particle size distribution, (b) TEM image showing well dispersed hexagonal crystalline platelets.(c) XRD trace showing a single ordered crystalline phase.

The efficiency of radioisotope incorporation into the LDH structure was determined to be ~75% through analysis of LDH wash solutions using a gamma-counter. The ^{57}Co incorporated into the nanoparticles was also found to be chemically stable, with TLC unable to bind and separate any of the incorporated ^{57}Co species.

Further TLC analysis of ^{57}Co leached from the nanoparticles in a range of different buffer solutions resulted in several key findings (Fig. 3):

- LDH nanoparticles are stable at pH 6-9.
- At pH 5 some initial breakdown (~20%) of LDH is evident.
- At pH 4 a large amount (>60%) of the nanoparticles undergo decomposition within 5 hours, and dissolution continues slowly after this time.

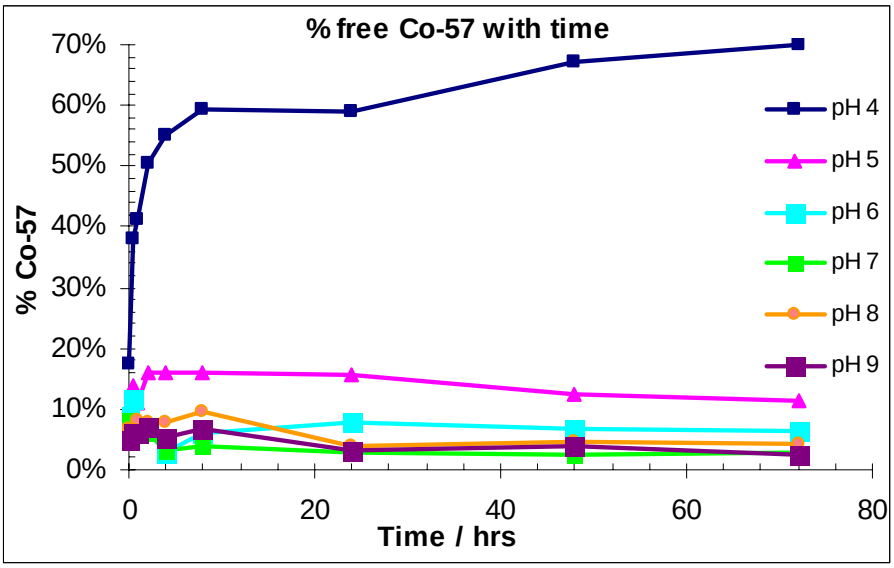

Figure 3: Compiled TLC results showing amount of free Co-57 leached from LDH structure over a range of pH= 3-9, with respect to time.

XRD studies, supports the TLC results with a greatly diminished degree crystalline layered structure evident with increasing incubation time at pH 4, suggesting decomposition of the nanoparticles (Fig. 4). TEM images confirm TLC and XRD results with an increasing amount of amorphous and fractured LDH material present with increasing incubation time in the pH 4 buffer (Fig. 4).

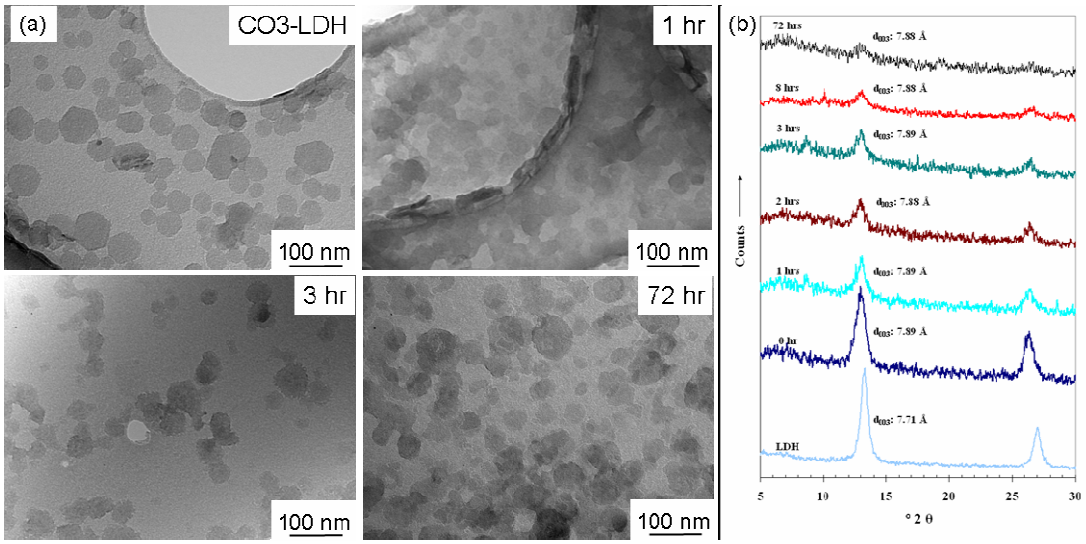

Figure 4(a) TEM images of LDH nanoparticles after differing time intervals in a pH 4 buffer (0.1 M sodium acetate). An increased degree of hexagonal platelet destruction and amorphous material is evident with increasing incubation time, (b) XRD patterns show a greatly diminished degree of crystalline LDH layered structure evident with increasing incubation time at pH 4, suggesting decomposition of the nanoparticles.

Summary / Conclusions

We have shown, for the first time, the successful use of radioisotopic labelling of clay nanoparticles to quantitatively follow the structural decomposition of LDHs at a range of biologically relevant pH levels. The incorporated Co-57 has been observed to mimic the decomposition behaviour of the LDH nanoparticles. The use of radioisotopes for labelling LDHs provides a potential novel and non-invasive methodology for following the biological fate of the nanoparticles in both *in vitro* and *in vivo* studies. The effect of charge and structure on biostability, interaction with biomolecules, biodistribution, bioretention and bioaccumulation will be investigated in further studies.

References

1. Nanotechnology, ATSE Focus No 124. 2002, Australian Academy of Technological Sciences and Engineering.
2. Australian Nanotechnology – Capabilities and Commercial Potential, in Invest Australia. 2005.
3. Foresight Nanotechnology Challenges. 2005, Foresight Nanotech Institute.
4. G. Oberdorster, E. Oberdorster, J. Oberdorster, Environmental Health Perspectives, 113, 7, 2005.
5. G. Oberdorster et al., Particle and Fibre Toxicology 2, 8, 2005.
6. Adventitious Products of Nanotechnologies. 2005, SCENIHR, European Commission.
7. Boulter, D., Critical Reviews in Plant Science, 16, 3, 1997.
8. Utracki, L.A., M. Sepehr, and E. Boccaleri, Polymers for Advanced Technologies,18, 1, 2007.
9. Z. P. Xu et al., Journal of the American Chemical Society 128, 36, 2006.

Preliminary paleolimnological data from a Santiago Island coastal lagoon, Galapagos Archipelago, Ecuador

Ashley Natt [1] , Simon Haberle [2] , Geraldine Jacobsen [3], John Tibby [4]
[1]*Environmental Biology, University of Adelaide, South Australia*
[2]*Department of Archaeology and Natural History, ANU, Canberra, ACT*
[3]*Australian Nuclear Science and Technology Organisation, Menai NSW*
[4] *Geographical and Environmental Studies, University of Adelaide, South Australia*

The Galapagos Islands are arguably the most famous islands in the world. This fame derives from the Islands' rich biological history and unique locality that provides opportunities for research in the fields of evolution, geomorphology and biodiversity. Furthermore, the unique geographical location of the archipelago has in the past and continues to provide excellent potential for palaeoclimatology, palaeolimnology and palaeoecology. In particular the location of the islands within what is essentially the heart of the ENSO region ensures the islands are frequently influenced by El Niño driven precipitation events. These El Niño precipitation events are extremely influential, given that the islands location within the Pacific Equatorial Dry Zone (PEDZ) ensures the islands have a semi-arid climate (<500 m above sea level). Due to the influential nature of El Niño variability in the Galapagos, the numerous saline to hyper-saline coastal lagoons throughout the archipelago have the potential of recording past hydrological changes associated with El Niño-related climate variability. Furthermore, the influence of humans via the introduction of goats and burning may have influenced erosion rates in the catchment.

Preliminary multi-proxy analysis of a laminated sediment sequence raised from the Espumilla lagoon system, Santiago Island, will be presented. The data includes a ^{14}C AMS radiocarbon chronology, fossil diatom analysis, magnetic susceptibility and 2mm resolution ITRAX x-ray fluorescence geochemistry. The preliminary results show that the sediment core raised from this site has vast potential for reconstructing El Niño driven rainfall over the past 2500 calibrated years BP, while at the same time revealing a detailed and interesting history of the evolution of this ecologically significant lagoon system.

Mechanical properties of cortical bone allografts irradiated at a series of gamma doses from 5 to 25 kGy

Huynh Nguyen [1], Michael Bennet [1], David AF Morgan[2], Mark R Forwood [1]
[1] *School of Biomedical Sciences – The University of Queensland*
[2] *Brisbane Private Hospital and Queensland Bone Bank*

Introduction

In an effort to eliminate the risk of contamination of bone allografts to an acceptable sterility assurance level (SAL), gamma irradiation at 25 kGy (standard dose) is commonly used as a terminal sterilisation. It is common knowledge that the dose can provide the SAL of a product to 10^{-6}, the acceptable level for implanted products. Recently, publications indicate that the bioburden of processed bone allografts is relatively and consistently low. Obviously, the lower bioburden, the lower radiation sterilisation dose that can be applied to get a required SAL 10^{-6}.

When irradiated at 25 kGy (standard dose), bone strength may be degraded 20 – 30% compared to non-irradiated groups [1]. This pattern of failure is consistently observed [2-4]. However, the evidences for mechanical damage when bone is irradiated at lower doses such as 15 or 10 kGy are few and not very clearly defined. In support of dose reduction, this project aim to investigate the changes in mechanical properties of cortical bone allografts irradiated at series of incremental doses from 5 to 25 kGy.

Material and method

Bone material

Sixteen femoral shafts were sawed into 48 cortical portions (4cm in length). Each portion was then cleaved to get 6 cortical bone beams. They were then machined and polished to a final size of 40x4x2mm. Beams from each portion were allocated to 6 groups, one control (0 kGy), and five others irradiated at 5, 10, 15, 20, and 25 kGy. Bone samples were always stored at -75^0C, except when being processed. All bone samples obtained at Queensland Bone Bank follow its standard operating procedures, and the project was approved by Queensland Health Scientific Services.

Three point bending test

Bones were tested according to previously published method [5]. Specimens were placed on two rigid brass supports 24mm apart and tested in three-point loading, with the actuator and its attached load-cell applying load to the mid-span. Actuator speed was 1mm/s. Force-displacement data was acquired using Wavemaker software (Instron, UK).

Data analysis

Load-displacement curves obtained from each sample test were accessed to determine structural properties (fig. 1)

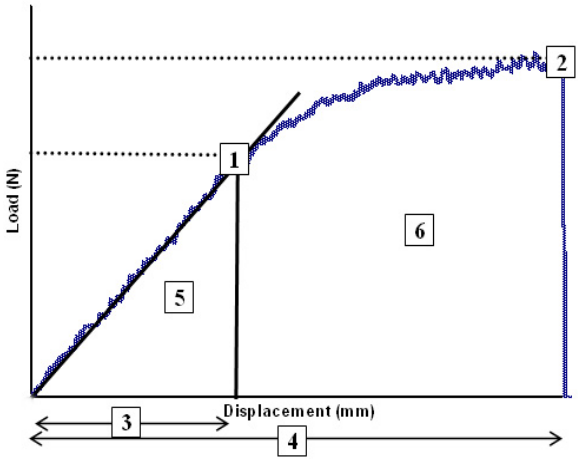

Figure 1: Load – Displacement curve

yield load (1), Fracture load (2), yield displacement (3), fracture displacements (4), work to yield (5), work to fracture (5+6)

Material properties were calculated as [6]:

$\delta = F(3l/2wt^3)$

$\varepsilon = d(6t/l^2)$

$E = S(l^3/4wt^3)$

$u = U(9/lwt)$

Where *δ: stress*

ε: strain

E: Elastic modulus

u: toughness modulus

F: Applied force

d: loader displacement

S: stiffness (F/d)

U: Work to failure

l: the span of the loader (24mm)

w: specimen width (4mm)

t: specimen thickness (2mm)

Statistical analysis

ANOVA was used to analyse the differences in mechanical properties among the groups. Where there were significant differences among groups, post hoc analysis was used to specify the differences. Differences are considered as significant if $p<0.05$.

Results and discussion

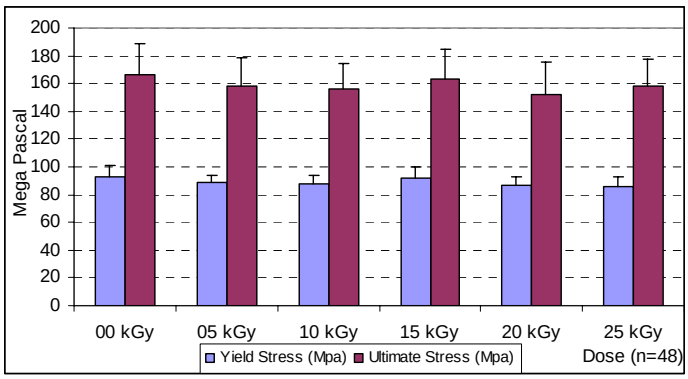

Figure 2: Yield and ultimate stresses of irradiated cortical bone were slightly affected by irradiation at "standard dose" ($p<0.05$)

Statistical analysis indicates that there was slight decrease in stress between control group and irradiated groups ($p<0.05$). The trend is the same in both yield and ultimate properties where stresses of irradiated bones were nearly 10 % lower than control bones (fig. 2).

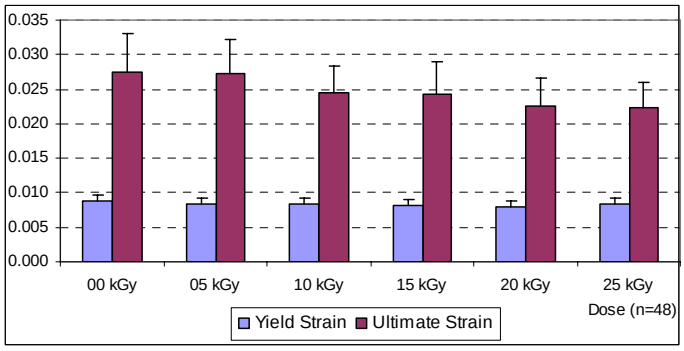

Figure 3: The ultimate strain of cortical bone is gamma dose- dependent ($p<0.001$)

However, while the deformation of bone at yield stress remained around 10 % lower in irradiated groups ($p<0.01$), this property at ultimate stress was dramatically decreased ($p<0.001$(fig. 3). When being irradiated at 10 or 15 kGy, bones still remained nearly 90 % of their ultimate strain compared to control conditions. But at 20 or 25 kGy of gamma dose, the ultimate strain was only 80 % compare to control group. This is due to a documented explanation that irradiated bones reduce their ability to absorb energy, and therefore less resistant to the stress.

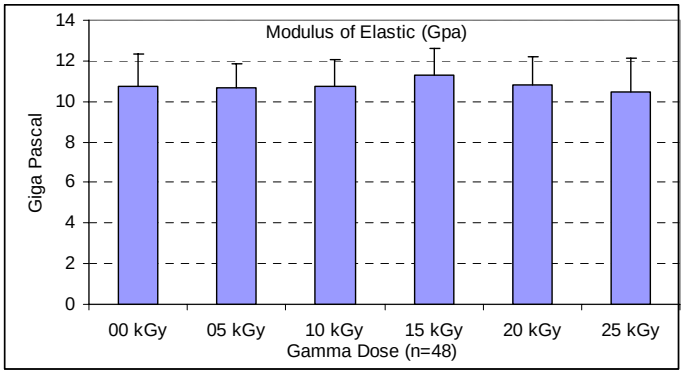

Figure 4: Modulus of elastic of bones was not changed when the gamma dose increased from 0 to 25 kGy ($p>0.05$)

Consequently, irradiated bone still remains it elasticity (fig. 4), but decreases it fracture energy or toughness (fig. 5). There is completely no statistical difference in modulus of elastic among irradiated and non-irradiated bone groups ($p>0.05$). In contrast, modulus of toughness was gamma dose-dependent. The toughness was decreased from 87% to 74% compare with control group when the dose increased from 15 to 25 kGy, respectively. Importantly, while the toughness difference between frozen-only group and 15 kGy group was not statistically significant ($p>0.005$), this difference between control and higher dose groups was highly significant ($p<0.001$). This may affect the working life of cortical bone allografts because the reduced toughness reflects a reduction in the ability to resist crack propagation, and the allografts are usually used to support weight bearing.

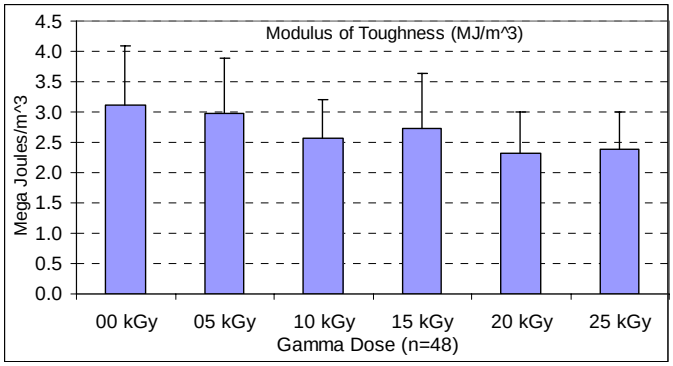

Figure 5: Toughness modulus of bone specimens significantly degraded when the gamma dose is increased ($p<0.001$)

Conclusion

Cortical bone irradiated at 'standard doses' degraded their plastic properties in static in vitro experiments, and therefore may reduce their weight bearing function when being implanted. However, bones irradiated at lower doses such as 10 or 15 kGy still retain their properties very close to control, fresh frozen, bones. Hence, the mechanical quality of bone allografts must be improved if lower doses approved for terminal sterilisation of bone allografts.

References

1. Currey, J.D., et al., *Effects of ionizing radiation on the mechanical properties of human bone.* Journal of Orthopaedic Research, 1997. 15(1): p. 111-117.
2. Akkus, O., R.M. Belaney, and P. Das, *Free radical scavenging alleviates the biomechanical impairment of gamma radiation sterilized bone tissue.* Journal of Orthopaedic Research, 2005. 23(4): p. 838.
3. Hamer, A.J., I. Stockley, and R.A. Elson, *Changes in allograft bone irradiated at different temperatures.* J Bone Joint Surg Br, 1999. 81(2): p. 342-4.
4. Cornu, O., et al., *Effect of freeze-drying and gamma irradiation on the mechanical properties of human cancellous bone.* Journal of Orthopaedic Research, 2000. 18(3): p. 426-431.
5. Benell, L.K., et al., *Age does not influence the bone response to treadmill exercise in female rats.* Medicine & Science in Sports & Exersise, 2002. 34(12): p. 1958-1965.
6. Cowin, C.S., ed. *Bone Mechanics Handbook*. 2001.

Superconducting and magnetic properties of $RuSr_2(Eu_{1.5}Ce_{0.5})Cu_2O_{10}$

R. Nigam *, A.V. Pan, and S.X. Dou
Institute for Superconducting and Electronic Materials, University of Wollongong, Northfields Avenue, NSW 2522, Australia.
**Corresponding author: rn393@uow.edu.au*

Superconductivity and magnetism were considered to be mutually exclusive phenomena before a region of coexistence was observed at very low temperatures in superconducting tertiary rare earth compounds (RRh_4B_4, RMo_6S_8, RMo_6Se_8[1], and RNi_2B_2C[2] systems where R=rare earth), $CeRh_{1-x}Co_xIn_5$, URhGe and $ZrZn_2$. The most recent discovery was the observation of coexistence of SC and magnetism in high temperature superconductors, called rutheno-cuprates. The two well known rutheno-cuprate materials are $RuSr_2R_{2-x}Ce_xCu_2O_{10}$, (Ru-1222)[3,4], and $RuSr_2RCu_2O_8$ (Ru-1212)[5,6] where R= Eu, Gd and Sm. In these compounds superconductivity appears when system is in ferromagnetic (FM) state hence they are called Superconducting ferromagnet **(SCFMs)**. In both Ru-1222 and Ru-1212 the magnetism is originated from RuO_2 sheet, or more precisely the RuO_6 octahedra and superconductivity is supposed to reside in CuO_2 planes. Both the superconducting and magnetic layers are practically decoupled which accounts for mutually exclusive yet coexisting nature of the two phenomenon. However, it casts doubts about the genuine coexistence of both the phenomena at a microscopic level. Ru-1222 system has much more complicated magnetic behaviour in comparison to Ru-1212. In contrast to single magnetic transition at 133 K in Ru-1212 system, Ru-1222 undergoes multiple magnetic transitions, nature and origin of which is still not clear, hence makes it rather much more difficult system to understand.

We studied polycrystalline samples of $RuSr_2Eu_{1.5}Ce_{0.5}Cu_2O_{10}$ with different sintering temperatures by performing X-Ray diffraction, dc magnetization, ac susceptibility and resistivity measurements. The sample of $RuSr_2Eu_{1.5}Ce_{0.5}Cu_2O_{10}$ (Ru-1222) was synthesized through a solid-state reaction route from the stoichiometric amounts of 99.99% pure RuO_2, $SrCO_3$, Eu_2O_3, CeO_2 and CuO. Sample was heat treated at 1000°C, 1020°C, 1040°C, 1060°C, and 1080°C for 12 hours with intermediate grinding. The sample was pressed into circular pellets. The pellets were then annealed in flowing oxygen at 600 ° C for 48 hours and subsequently cooled slowly over a span of another 24 hours down to room temperature. X-ray diffraction (XRD) patterns were measured by Philips PW1730 using Cu-K alpha radiation. The DC magnetic measurements were performed using Magnetic Property Measurement System (MPMS-XL, Quantum Design) in temperature range of 1.9-300 K. The four probe resistivity measurements were carried out using Physical Property Measurement System (PPMS, Quantum Design).

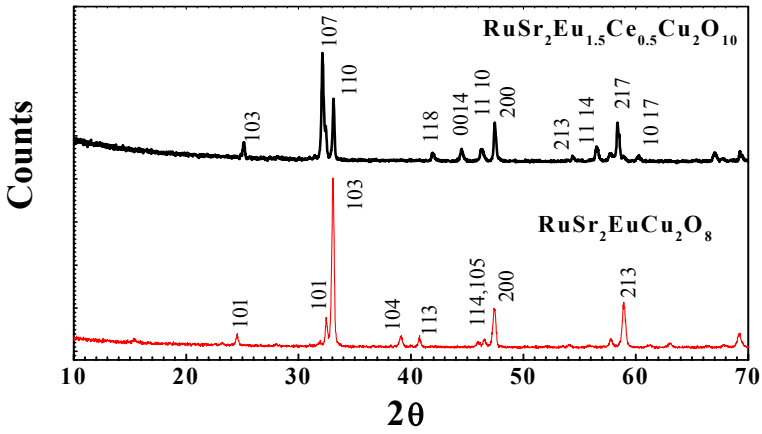

Fig. 1 X-Ray diffraction pattern of $RuSr_2Eu_{1.5}Ce_{0.5}Cu_2O_{10}$ (Ru-1222) and $RuSr_2EuCu_2O_8$ (Ru-1212).

Fig. 1 shows the XRD pattern of $RuSr_2Eu_{1.5}Ce_{0.5}Cu_2O_{10}$. The XRD shows that the sample is phase pure, but a small peak at $2\theta = 32°$ indicates the presence of some amount of $SrRuO_3$ phase. Ru-1222 has tetragonal structure belonging to I4/mmm space group, having lattice parameters a = b = 3.84398 and c = 28.5957.

Fig. 2 shows zero field cooled (ZFC) and field cooled (FC) dc magnetization curves. ZFC and FC curves exhibit a sharp rise at 91 K indicating ferromagnetic transition. As the temperature is further cooled a small kink (change is slope) in both ZFC and FC curves is observed at 28 K, which corresponds to the onset of superconductivity and is denoted as Tc^{onset}. In addition, a clear diamagnetic signal is observed below 15 K which indicates the superconducting property of the material. Thus, system undergoes superconducting transition in ferromagnetic state. Other important features of dc magnetization curve is the peak in ZFC curve (denoted as T_{cusp}) at 74 K followed by a large difference in ZFC and FC magnetizations and monotonous increase of FC curve with decrease in temperature. This irreversibility in ZFC and FC susceptibility is the signature of metastability. Interesting observation is that, although the pronounced irreversibility is observed below T_{cusp} a small branching in ZFC and FC curves could be seen in between 91 K and 160 K. This can be seen in the inset of Fig 2, which shows an enlarged view of dc magnetization curves above T_{cusp}. The appearance of irreversibility feature much above T_{cusp} indicates the presence of uncompensated spins, which bear dipolar interaction between them[7]. This uncompensated spin contribution may come from the minority phase present in the sample under test, i.e. $SrRuO_3$ phase. In our previous work, we have shown that the presence of minority $SrRuO_3$ and Ru-1212 phase in bulk Ru-1222 alters the structural, magnetic and transport properties of the system both in superconducting and normal state[8]. In order to understand the metastable magnetism in Ru-1222 system we carried out third harmonic ac susceptibility measurements. Spin glass state along with the ferromagnetic component exists below T_{cusp} in Ru-1222 system. Further discussion on this is beyond the scope of this article.

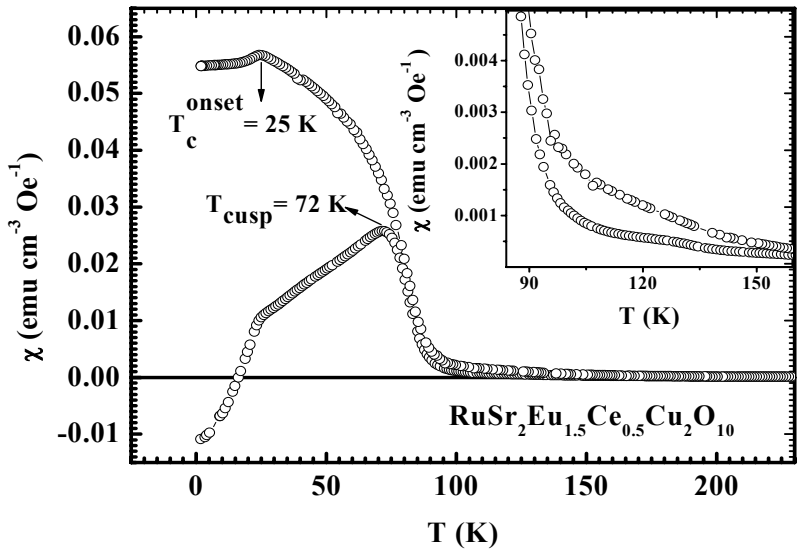

Fig. 2 ZFC and FC magnetization curves measured at applied field, H = 10 Oe. Inset shows enlarged view of ZFC- FC curve indicating the irreversibility observed at 90 K ≤ T ≤ 160 K.

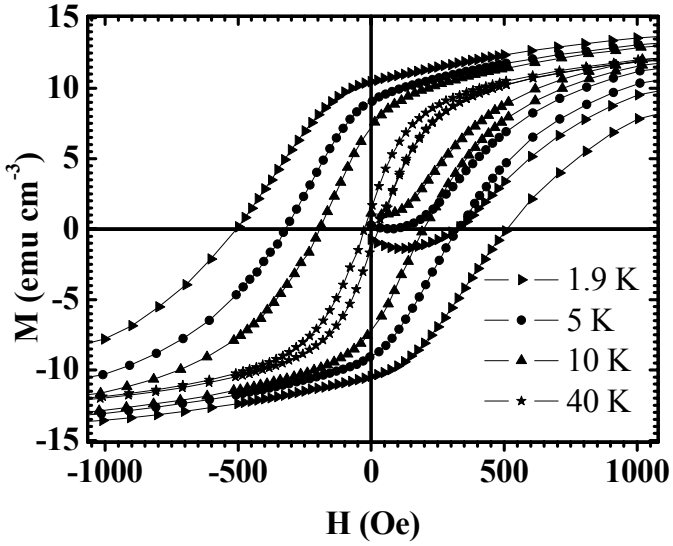

Fig. 3 Magnetization (M) verses applied field (H) curve measured at different temperatures.

To further investigate the coexistence of superconductivity and ferromagnetism in Ru-1222, the hysteresis loops were measured at different temperatures over an applied magnetic field of -5 T ≤ H ≤ 5 T. M-H curves in Fig. 2 shows a FM-like hysteresis loop at low temperatures along with a simultaneous negative magnetization at low applied fields, which is a diamagnetic signal typically for a superconducting state. Thus, the coexistence of superconductivity and ferromagnetism is clearly evident from M-H curves.

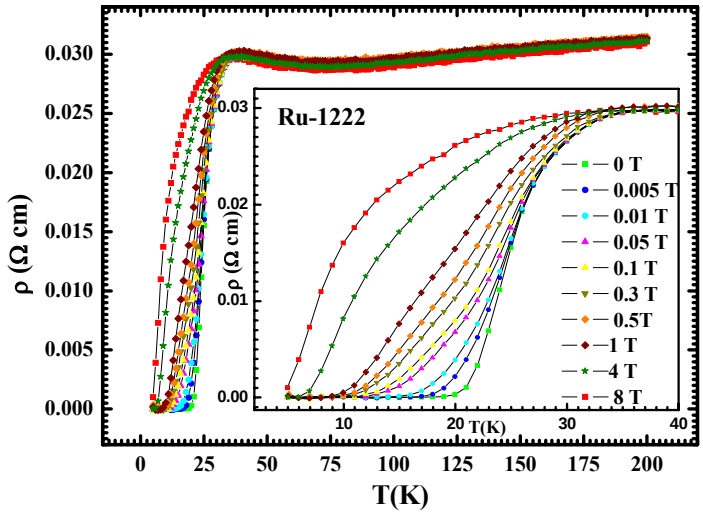

Fig. 4 Temperature dependence of resistivity of polycrystalline Ru-1222 measured at applied field H ≥ 8 T. Inset shows the enlarged view of the superconducting region.

Fig. 4 shows the temperature dependence of resistivity at applied magnetic field H ≥ 8 T. In the normal state, Ru-1222 shows a metallic behaviour. Below Tcusp = 75 K, a slight upturn in resistivity could be observed following which resistivity suddenly drops and the superconducting transition occurs close to T_c^{onset} = 35 K. For H = 0 T, zero resistivity is observed at T_c^0 = 21 K. With increase in applied field zero resistivity shifts to lower temperature and for H = 8 T although superconducting transition occurs but resistivity does not reach zero. The superconducting transition width (T_c^{onset}-T_c^0) is broad due to granular nature of high temperature superconductors according to which, first the grains become superconducting at higher temperature following that grain boundaries superconducts, as a result complete zero resistivity is obtained at a temperature lower than T_c^{onset}.

In this article we have presented the structural, magnetic, and transport properties of $RuSr_2Eu_{1.5}Ce_{0.5}Cu_2O_{10}$, which clearly depicts the coexistence of superconductivity and ferromagnetism in this compound.

For a review, see Topics in Curretn Physics, edited by Ø. Fischer and M.B. Maple (Springer-Verlag, New York, 1983), Vol. 32 and 34.

1 J.W.Lynn, et.al., Phys. Rev. B **55**, 6584 (1997).

2 I. Felner, U. Asaf, Y. Levi, and O. Millo, Phys. Rev. B **55**, R3374, (1997).

3 E. B Sonin, and I. Felner, Phys. Rev. B, **57**, 14 000, (1998).

4 C. Bernhard, et.al., Phys. Rev. B **59**, 14 099, (1999).

5 A.C MacLaughlin, et.al, Phy. Rev. B. **60**, 7512, (1999).

6 Sunil Nair, and A. Banerjee, Phys. Rev. Lett. **93**, 117204, (2004).

7 R.Nigam, A.V.Pan, S.X. Dou, J. Appl. Phys. **101**, 09G109 (2007)

Drying of a sol gel droplet suspended in a flowing atmosphere

G. J. Oberman *, T. W. Farrell *, E. Sizgek # and J. R. Bartlett
* *School of Mathematical Sciences, Queensland University of Technology*
# *Materials Division, Australian Nuclear Science and Technology Organisation*

Introduction

The spray drying of colloidal solutions, or sols, is of importance in numerous manufacturing applications. One important application is the production of nanoporous ceramic powders. In this project, the overall aim is to develop a mathematical model of this process in order to determine how changes in the chemistry within individual sol droplets, and in the drying conditions, alter the morphology and characteristics of the resulting powders. In particular, we are interested in the spray drying process applied during the creation of Synroc™[1], a synthetic rock structure that is used to encapsulate high level liquid waste.

The sol which is used in the spray drying process we are modelling consists of titanium, zirconium, and aluminium oxides, suspended in a solution of water, aluminium nitrate and nitric acid. This sol is known as the TZA sol[1].

The spray drying process involves four distinct phases. First, the atomised sol is released into the drying chamber. Once in the chamber, the droplets evaporate until colloid at the surface solidifies to form a crust. Third; liquid is evaporated through the crust and this causes the crust to thicken. Finally, when most of the liquid has been evaporated, the microsphere is heated until it exits the drying chamber. This process can lead to a variety of morphologies, the most desirable being a solid sphere. Less desirable morphologies include tori and hollow spheres, the latter of which are particularly undesirable as nuclear waste material may sit within the hollow rather than bonding with the chemical structure of the substance. The mathematical model developed in this project aims to capture the second stage of this process, where the morphology is decided.

One approach to capturing the coagulation of sols is to use a critical coagulation concentration. While this approach is valid for static processes, it is not appropriate for the model we are developing. As such, we instead model the colloidal behaviour more directly, by examining DLVO theory[2] and interaction potentials of colloidal particles, as well as reaction kinetics.

In developing an overall mathematical model of sol droplet drying we must ensure that the relevant physical and chemical processes are accounted for in a consistent manner. To do this we have developed the model in stages, beginning with the simplest related case that could be considered – namely, a pure liquid droplet evaporating in an atmosphere consisting only of its own vapour[3]. This model allowed for consideration of such issues as evaporative boundary conditions and capturing of the moving boundary. This model was then extended to account for a second gaseous species acting as an atmospheric gas[4], and then extended again to capture some elements of the flow of the atmosphere past the droplet, while maintaining spherical symmetry. From these models came a framework from which the colloidal properties could be added. Further details on these models follow.

Intermediate Models

As mentioned above, it was necessary to build the model in stages. The first model, involving a pure liquid droplet evaporating in its own vapour[3], enabled

consideration in detail of evaporative conditions at the liquid/gas boundary. In addition, it facilitated the identification of an appropriate method of handling the moving boundary of the droplet. This model showed realistic behaviour, and agreed qualitatively with well-known empirical results.

The next model then introduced a second, atmospheric gas into the system, forming a model of a pure liquid droplet evaporating in a binary atmosphere[4]. This model involved the process of binary gas diffusion, a process not seen in the previous model as the vapour phase was pure. It also required some alterations to boundary conditions found in the previous model.

Boundary conditions found in this "binary gas" model include continuity of temperature at the liquid-gas interface, conservation of mass for the liquid/vapour and for the atmospheric gas, conservation of thermal energy for supplying the latent heat of vaporisation of water, an equation that expresses the force balance through pressure, surface tension, and evaporative force, and a generalised form of the Clapeyron equation[5], which expresses equilibrium properties of evaporation.

Throughout these models, spherical symmetry is assumed, so that the system essentially becomes one-dimensional in space. This was useful for a droplet suspended in a quiescent gas, but in order to introduce gas flow effects, some non-symmetric behaviour needed to be introduced. To do this, a simplification was made in which the flow behaved as a Stokes flow[6] around a sphere, and it was assumed that this flow did not affect the flow due to evaporation directly. This resulted in a method of determining the net effect of the Stokes flow at a particular distance from the droplet. Upon integration, an expression of this Stokes flow effect in a spherically symmetric framework is obtained. The addition of this Stokes flow formed the third model of the evaporation of a liquid droplet in a flowing binary atmosphere.

The models included the assumption that each phase was internally in equilibrium initially, as though an impermeable sheath were placed around the droplet, and removed at time t=0. One side-effect of this assumption was that, at early times, either explosive evaporation or implosive condensation was observed, separately from the net evaporation, as the temperature of the droplet was brought to the wet bulb temperature. While the effect of the assumption is not entirely accurate, it emulates the effect of suddenly releasing the droplet into the chamber, and must be captured in order to have a realistic model of the process. This behaviour can be seen in Figure 1.

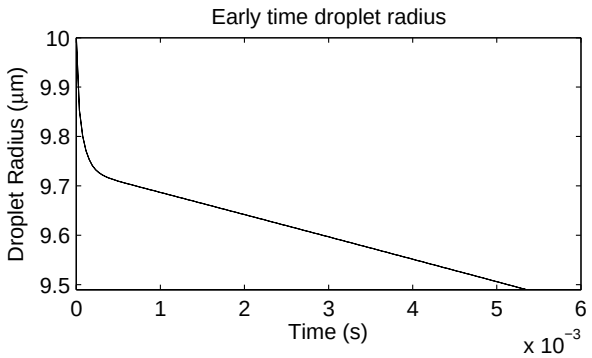

Figure 1: Plot of radius of droplet at early times, exhibiting explosive evaporation

The results of the binary gas model solver written in MATLAB have been compared with experimental data, and showed good agreement. The results have also been compared with data for colloid droplets, and these results showed reasonable

agreement for a large part of the evaporation process, deviating significantly at late times when the droplet begins to coagulate at a rapid pace, as can be seen in Figure 2.

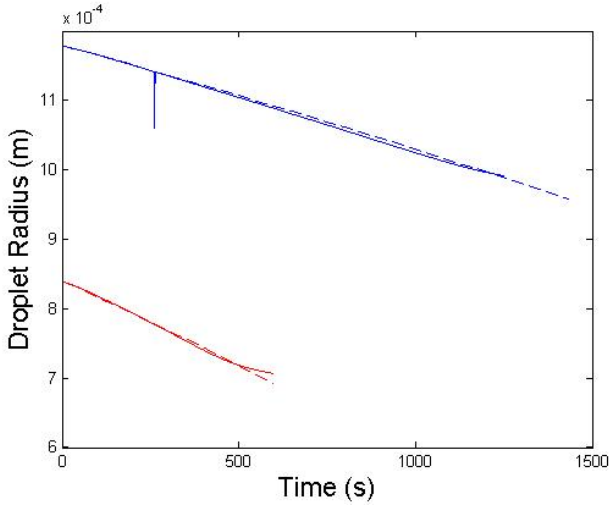

Figure 2: Comparison of experimental (—) and predicted (– –) colloid droplet radii for two droplets

Colloid Modelling

Now attention is turned to the colloid within the droplet. The colloid consists of a solid oxide component, an acid, and a salt. Both the acid and the salt dissociate in the water of the droplet, resulting in three ions – aluminium, hydrogen, and nitrate. It is these ions that produce the double-layer charge common to colloids. As such, their interaction must be captured.

In order to simplify the model, a number of assumptions are made. Local conservation of charge is assumed, meaning that, on the 'macroscopic' scale, the charges balance – this is not, however, true on the scale of the colloid particles. Conservation of volume is also assumed, as this is a system of liquid and solid components, and all components have approximately constant densities. These assumptions allow the five components of the sol – namely water, colloid, aluminium, hydrogen, and nitrate – to be modelled as though they were three components – water, colloid, and electrolyte.

The DLVO theory of colloids[2] provides a method of determining the interaction energy between two isolated colloid particles, given the distance between them and other important variables. However, this model requires the net interaction energy on any particular colloid particle due to all other particles in the droplet. In order to facilitate this, the inter-particle interaction energy is integrated over the entire droplet as:

$$U_c(\mathbf{r}) = \frac{1}{m_c} \iiint_{droplet} \frac{\rho_c(\mathbf{r})}{m_c} U_p(|\mathbf{r}-\mathbf{r}'|) dV'$$

where U_c is the specific net interaction energy, and $U_p(|\mathbf{r}-\mathbf{r}'|)$ is the inter-particle interaction energy between particles located at positions $\mathbf{r}$ and $\mathbf{r}'$. This expression can be rearranged to eventually arrive at a form that is conducive to computational methods.

The model equations themselves separate out into three sets. The first set is the continuity equations. The second set is the equation derived from the aforementioned net interaction energy equation. The final set consists of the momentum balance equations[6], and it is here that such effects as the Stokes force on the colloid due to its motion through the water and diffusion forces are incorporated into the model.

Additional boundary conditions representing conservation of mass for the colloid and electrolyte components are applied, in addition to those found in the pure liquid models, indicating that no colloid or electrolyte passes through the surface of the droplet. .

To date, we have developed a model for the process of the drying of sol gel droplets, and work is ongoing on producing a solver, to be written in MATLAB, that will make use of finite volume methods to express the system as a system of nonlinear equations, and will use a Newton solver to find the solution. The three sets of equations are solved in separate steps, and the steps are repeated until the resulting numbers converge to consistent values. It will output the distributions of species within the droplet over time, as well as the droplet radius. The code will run until the moment at which the colloid coagulates to form a thin shell, at which point the density of colloid particles will be used to determine the final morphology of the droplet.

References

1. Sizgek, E., J.R. Bartlett, and M.P. Brungs, *Production of Titanate Micropheres by Sol-Gel and Spray-Drying.* Journal of Sol-Gel Science and Technology, 1998. **13**(1-3): p. 1011-1016.
2. Shaw, D.J., *Introduction to Colloid and Surface Chemistry*. 4th ed. ed. 1992, Boston: Oxford.
3. Oberman, G.J., T.W. Farrell, and E. Sizgek, *Drying of a liquid droplet suspended in its own vapour.* ANZIAM J., 2005. **46(E)**: p. C1155-C1169.
4. Oberman, G.J., et al. *Drying of a Liquid Droplet Suspended in a Binary Atmosphere*. in *Fifth International Conference on CFD in the Process Industries*. 2006. Melbourne, Australia.
5. Lock, G.S.H., *Latent Heat Transfer*. Oxford Engineering Science Series, ed. J.M. Brady, et al. 1994, New York, NY: Oxford University Press.
6. Bird, R.B., W.E. Stewart, and E.N. Lightfoot, *Transport Phenomena*. 1960, Madison, WI: John Wiley and Sons, Inc.

Surface structure analysis of Ni/Cu(100), Fe/Cu(100) and Ni/Fe/Cu(100)

D. J. O'Connor [1], P.D. Dastoor [1], D.A. MacLaren [2]
[1] *School of Mathematical and Physical Sciences, University of Newcastle, NSW 2308*
[2] *Dept. of Physics and Astronomy, The University of Glasgow*

Medium Energy Ion Scattering is a mature technique designed to determine the structure and composition of the outermost atomic layers. With the latest techniques allowing accurate prediction of line profiles and a computer simulation, VEGAS, it is possible to monitor thin film growth at submonolayer level and determine the effect on surface relaxation layer by layer.

In this sequenced study, the final goal is to determine the growth behaviour of the dual deposition of Ni and Fe, but first a careful study was undertaken of the individual depositions was undertaken. This revealed an anomaly associated with a previous study of the Fe/Cu(100) surface by Helium Atom Scattering. The findings of the MEIS study has given greater insight to the HAS technique which will improve its application in the future.

More detailed analysis, has allowed the determination of the level of damage in these ultrathin films.

Helium ion microscope – high resolution, high contrast microscopy for nanotechnology

D. J. O'Connor
School of Mathematical and Physical Sciences, University of Newcastle, NSW 2308

The Helium Ion Microscope is the marriage of a crystal tip field ionisation source and an electron microscope column to attain high resolution images of surface and interfaces. The high brightness and small spatial distribution of the field ionisation source is used to create a 20keV He ion beam which is refocused onto surfaces. The higher mass of the projectile and the nature of secondary electron emission for energetic ions leads to a potential lateral resolution of 0.25nm though so far the best obtained is 0.8nm.

The different electron emission resulting from ions compared to electrons leads to greater contrast in secondary electron mode and it is possible to image both surface and subsurface simultaneously. In lithography applications, the incorporation of He into a surface has no chemical impact to the subsurface region compared to other ion beam etching processes.

This instrument is still under development by Carl Zeiss SMT, Inc and new features incorporating chemical identification via elastic particle scattering are expected to be part of future options.

Depth-profiling of thermal dissociation of Ti_3SiC_2 in vacuum

W. K. Pang * and I. M. Low
Centre for Materials Research, Department of Imaging and Applied Physics, Curtin University of Technology, GPO Box U1987, W.A. 6845
**email: weikong.pang@postgrad.curtin.edu.au*

Abstracts

Ternary carbides, such as Ti_3SiC_2, are susceptible to surface thermal decomposition at high temperature forming TiC_x and $Ti_5Si_3C_x$. The phase relations and properties of thermal decomposition of Ti_3SiC_2 in vacuum up to 1500 °C have been characterized by grazing-incidence synchrotron radiation diffraction (GISRD) and secondary-ions mass spectroscopy (SIMS). GISRD and SIMS have revealed a graded distribution of phases at the near-surface of thermally dissociated Ti_3SiC_2 and the compositional distribution is both temperature and time dependent.

Introduction

Many attempts have been made to produce new materials with a combination of ductility, conductivity and machinability of metals and the high strength, modulus and superior high-temperature-oxidation resistance of ceramics. Ternary carbides, such as Ti_3SiC_2 and Ti_3AlC_2, are layered compounds belonging to a family of ternary layered compounds with the general formula: $M_{n+1}AX_n$, where n is 1, 2 or 3, M is an early transition metal, A is an A-group (mainly group IIIA and IVA) element, and X is either carbon or nitrogen [1-11]. For instance, Ti_3SiC_2 has high toughness (6–11 MPa $m^{1/2}$), high Young's modulus (~320 GPa), low hardness (~ 4 GPa), and moderate flexural strength (260–600 MPa) [2-5]. Furthermore, it exhibits plasticity at high temperature, good electrical conductivity, high thermal shock resistance, and easy machinability[6-9]. The salient combination of properties makes ternary carbides ideal candidate materials for high-temperature applications.

However, ternary carbides (e.g. Ti_3SiC_2) are susceptible to surface thermal decomposition at ~1400 °C in inert environments forming TiC_x and $Ti_5Si_3C_x$ [11-12]. The chemistry and mechanism of dissociation processes involved are not fully understood. In this study, the techniques of grazing-incidence synchrotron radiation diffraction (GISRD) and secondary-ions mass spectrometry (SIMS) were used to investigate the processes of thermal dissociation of Ti_3SiC_2 in vacuum and the associated phase relations.

Experimental

Commercial samples, Ti_3SiC_2, were supplied by Kanthal AB of Sweden. The samples were sliced into smaller pieces and annealed in vacuum at 1300 °C, 1400 °C, 1450 °C and 1500 °C, respectively. The annealed samples were used in SIMS experiment to depth-profile the near-surface elemental composition vacuum-annealed Ti_3SiC_2. The near-surface composition of Ti, C, Si, and TiC was analysed using a Cameca Ims5f SIMS. A Cs^+ ion beam of 5.5keV impact energy was employed. Typical beam currents ranged from 50 to 150 nA and the beam was scanned across areas of 250 × 250μm^2. Secondary ions were accepted from a circular analysis area on the sample limited to a diameter of 55μm by a combination of lens and aperture settings.

Two slices of Ti_3SiC_2 were annealed in vacuum at 1500 °C for 8 and 12 h and they were used in GISRD experiment to study the effect of soaking time on the thermal dissociation of Ti_3SiC_2. A wavelength of 0.7 Å was used and the diffraction patterns

were recorded over a 2-theta range of 3 to 90.he fiducia. Two image plates were used and the exposure time was 10 min.

Results and Discussion

Analysis of SIMS Data

SIMS analysis reveals the existence of a graded distribution of phases at the near-surface of thermally dissociated Ti_3SiC_2 at various annealing temperatures (Fig. 1).

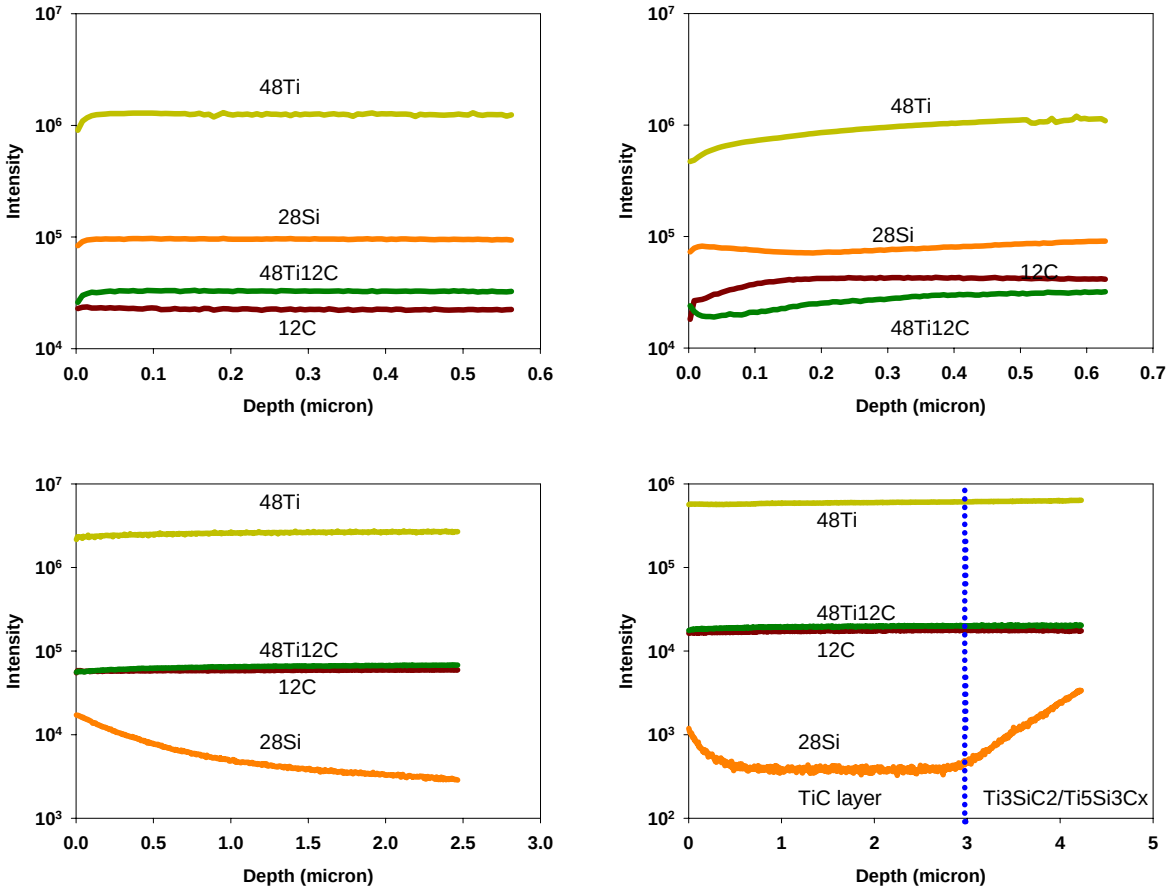

Figure 1: Intensity of secondary-ions vs. sputtered depth of vacuum-treated Ti_3SiC_2 at (a) 1300 °C, (b) 1400 °C, (c) 1450 °C, and (d) 1500 °C, respectively.

At 1300°C, the detected intensities of elements were fairly constant which indicates no thermal dissociation. However, these intensities start to vary with depth at 1400°C which suggests that Ti_3SiC_2 has commenced to dissociate, forming most probably $Ti_5Si_3C_X$. In other words, Ti_3SiC_2 is not susceptible to thermal dissociation up to 1300 °C but dissociates to $Ti_5Si_3C_X$ at 1400°C. At 1450°C, a near-surface layer of TiC_x formed as evidenced by the low intensity of silicon. It is believed that the low silicon signal results from the lost of silicon from the surface of Ti_3SiC_2 when it is vacuum-annealed at elevated temperature This hypothesis is supported by the decomposition model proposed by Emmerlich et al. (2007).[12] Based on this model, Ti_3SiC_2 decomposition is initiated by out-diffusion and entropy-driven evaporation of Si from the top surface toward vacuum during annealing. The Si out-diffusion is due to its low bond strength. Si is partially metallically bonded to Ti(I) (Ti atoms adjacent to Si)[13].

In other words, there is a TiC_x layer forming on the surface of thermally dissociated Ti_3SiC_2 at 1450°C.

At 1500 °C, an increase of Si signal is observed at the depth of ~3 micron which can be attributed to the existence of a boundary between the surface TiC layer and the inner $Ti_5Si_3C_X$ /Ti_3SiC_2 layer. Thus, a graded distribution of phases at the near-surface of thermally dissociated Ti_3SiC_2 was observed.

Analysis of GISRD Data

The diffraction patterns at various grazing angles or depths for Ti_3SiC_3 vacuum-annealed at 1500°C for various times are shown in Figure 2. The changes in peak intensity are observed at different depths.

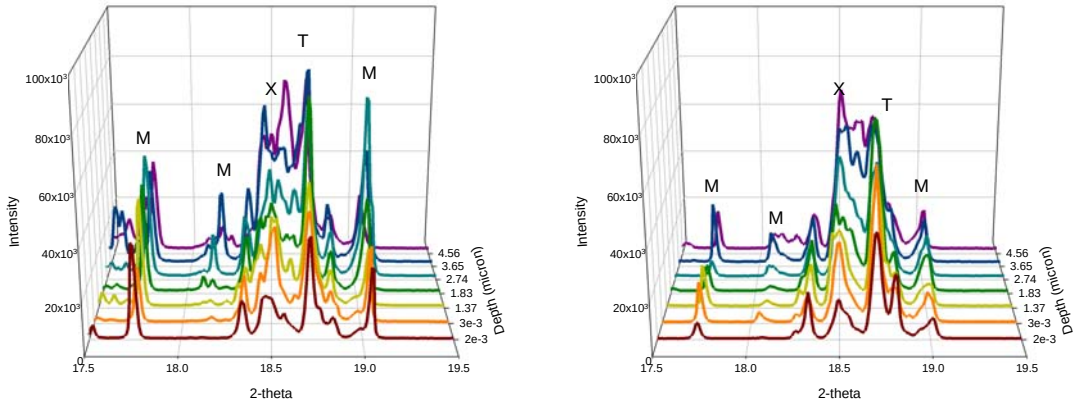

(a) (b)

Figure 2: Synchrotron radiation diffraction patterns of thermally dissociated Ti_3SiC_2 at 1500 °C for (a) 8 hours and (b) 12 hours., [Legends: M: Ti_3SiC_2 , X: $Ti_5Si_3C_x$ and T: TiC_x].

After annealing in vacuum for 8 hours, Ti_3SiC_2 was thermal dissociated to $Ti_5Si_3C_x$ and TiC_x at the near-surface. For both TiC_x and $Ti_5Si_3C_x$, peak splitting was observed which may be attributed to the presence of lattice defects or crystal disorder.

Due to the evaporation of Si, twinned Ti_3C_2 slabs formed and relaxed towards each other[12]. The redistribution of C was involved in the relaxation process. This process is in agreement with the known stability regime of TiC_x (x = 0.97–0.47)[12]. Therefore, homogenization in the C content to form $TiC_{0.67}$ is what can be expected.

As Ti_3SiC_2 experienced an extended 12-hour annealing in vacuum, the peak intensity of Ti_3SiC_2 was reduced when compared to the 8 h sample. This suggests that the process of thermal dissociation of Ti_3SiC_2 is time-dependent. At longer soaking time in vacuum heat-treatment, Ti_3SiC_2 will be more thermally dissociated to form $Ti_5Si_3C_x$ and TiC_x.

Conclusions

SIMS results revealed that Ti_3SiC_2 is not susceptible to thermal dissociation up to 1300°C but commences at 1400°C to form $Ti_5Si_3C_x$ initially and TiC_x at 1450°C. At 1500°C, the TiC_x layer formed was ~3μm thick. GISRD results indicated showed the existence of lattice defects in TiC_x and $Ti_5Si_3C_x$. The process of thermal dissociation of Ti_3SiC_2 is both temperature- and time-dependent.

References

[1] Barsoum, M. W. Prog. Solid State Chem. 28, 201 (2000).
[2] Palmquist, J. -P. , Li, S., Persson, P. O. A., Emmerlich, J., Wilhelmsson, O., Hogberg, H., Katsnelson, M. I., Johansson, B., Ahuja, R., Eriksson, O., Hultman, L. and Jansson, U. Phys. Rev. B 70, 165401 (2004).
[3] Barsoum, M. W., Brodkin, D. and El-Raghy, T. Scripta Mater. 36, **5** 535 (2000)
[4] Low, I. M. J. Euro Ceram. Soc. 18, 709 (1998)
[5] Gao, N. F., Miyamoto, Y., and Zhang, D. J. Mater. Sci. 34, 4385 (1999).
[6] Zhou, Y. C. and Sun, Z. M. Mater. Res. Innov. 2, 360 (2004).
[7] Kisi, E. H., Crossley, J. A. A., Myhra, S. and Barsoum, M. W. J. Phys. Chem. Solids 59, **9** 1437 (1998).
[8] Barsoum, M. W., El-Raghy, T., Rawn, C. J., Porter, W. D., Wang, H., Payzant, E. A. and Hubbard, C.R. J. Phys. Chem. Solids 60, 429 (1997).
[9] Zhou, Y. C. and Sun, Z. M. J. Phys. Cond. Matt. 12, 457 (2007).
[10] Low, I. M. Mater. Lett. 58, 927 (2004).
[11] Low, I. M., Oo, Z. and Prince, K. E. J. Am. Ceram. Soc. 90, 2610 (2007).
[12] Emmerlich, J., Music, D., Eklund, P., Wilhelmsson, O., Jansson, U., Schneider, J. M., Ho¨gberg, H., Hultman. L. Acta Mater. 55, 1479 (2007)
[13] Zhou, Y. and Sun, Z. J. Phys.: Condens. Matter. 12, L457 (1969)

Deposition of high quality metal and metal oxide thin films using a filtered cathodic vacuum arc

J. G. Partridge, N. Abaffy, M. Field, J. Du Plessis and D. G. McCulloch
Applied Physics, RMIT University, 124 LaTrobe Street, Melbourne, Australia
jim.partridge@rmit.edu.au

A Filtered Cathodic Vacuum Arc (FCVA) system has been used to produce metal oxides for electronic, optical and sensing components. The morphology and electrical characteristics of these films were tuned by changing substrate bias conditions and system inlet gas (Ar/O) flows. Atomic force microscopy, spectroscopic ellipsometry, X-ray photoelectron spectroscopy and electron microscopy have been used to characterise tungsten oxide, tin oxide, aluminium oxide and titanium oxide layers produced in the FCVA. In addition, ultra-thin metallic layers have been produced for use in optically absorbent layers. AFM, in-situ electrical conductivity and ex-situ low-temperature electrical conductivity measurements have shown that continuous aluminium layers of less than 10nm thickness can be produced with RMS roughness <0.2nm and conductivities within an order of magnitude of the bulk value.

Thermoluminescence spectra of quartz from single crystals

J.R. Prescott, D.F, Creighton
School of Chemistry and Physics, University of Adelaide, South Australia 5005
john.prescott@adelaide.edu.au

Introduction

For some years the Archaeometry Research Group has been studying the luminescence properties of quartz and feldspar, which provide the main element of the "clock" for luminescence dating. Samples for dating are typically drawn from sedimentary deposits and comprise either small assemblages of undifferentiated grains, or single grains from a variety of provenances. In luminescence dating, the sample is stimulated to emit light and the methodology used is determined by the wavelength of that light. Effective protocols are therefore assisted by better knowledge of the emission spectrum and the conditions that stimulate it. It is not surprising that the intensity of emission of individual grains from undifferentiated samples varies widely from grain to grain and is known to be often log-normal. There is some evidence that spectra from individual grains differ from one another. The present project is designed to examine these questions by studying single grains extracted from single, well-formed crystals, as an indicator of natural variability of intensity and spectrum. The present project is primarily directed towards understanding the luminescence of quartz and, in particular, whether trace elements in quartz affect, or perhaps determine, the spectrum. We have also been interested in feldspars, which are aluminosilicates of alkali and alkali-earths. The latter show a great variety of spectra, depending on the composition (Prescott and Fox 1993).

Methods

The Physical Archaeometry Group uses a Fourier-transform thermoluminescence spectrometer, of our own design and construction, to measure spectral intensity as a function of both temperature and wavenumber or wavelength (Prescott *et al.* 1988). It has a very high sensitivity and lends itself well to single-grain studies. It has recently been identified as the moist sensitive instrument of its kind. The results can be displayed as a contour diagram or an isometric plot, showing luminous intensity as a function of wavenumber and temperature, commonly referred to as a "3-D spectrum".

Such displays show well-defined intensity peaks. The temperatures of the peaks are related to the electron traps in the crystal, and the wavelengths are determined by the luminescence centres. At any given temperature there may be emission at more than one wavelength and *vice versa.* Because of the way the spectrometer works, the output is expressed in terms of wavenumber rather than the more-familiar wavelength. In-so-far-as the wavenumber is proportional to the energy of the corresponding photon, it relates somewhat more closely than wavelength to the underlying physics of the problem. The spectrometer covers a nominal wavelength range 250-720nm (5.0-1.7eV) from 50-500^{o}C. However, because of incandescence of the sample at the red end of the spectrum at the higher temperatures, most of the measurements are made with an optical cutoff at 660nm and limited to an upper temperature of 375^{o}C.

At the time of writing, we have measured the spectra of "bulk" samples, separated by crushing, from seventeen well-formed single quartz crystals of known provenance and six samples of undifferentiated quartz grains from geological field sites. We have also remeasured spectra from two feldspars that we have previously studied in a different context (Prescott and Fox 1993). All samples were etched in hydrofluoric acid before

measurement and field quartz samples were submitted to density separation at a specific gravity of 2.67 to remove heavy impurities (at 2.65, quartz floats). For single *grain* (as opposed to single *crystal*) measurements, the sample was sieved and the 300-350 μm fraction used. For a few of the samples, the composition (including trace elements) was known from earlier work. Unfortunately, the unavailability of OPAL at Lucas Heights for neutron activation analysis has meant that this is not yet known for most of the samples.

Measurements

General

We have obtained 3-D spectra from all samples using 5 mg aliquots; these contain about 1000 grains of various sizes. The specimens of single crystals are mostly clear and colourless, from a variety of provenances. However, some coloured specimens are included: amethyst, citrine, rose, green, blue and smoky. Bulk spectra from the latter group are of lower intensity than the clear crystals and show variations in spectra. We have not analysed these in details nor looked for correlations with trace elements, since the first priority was to identify samples suitable for single-grain spectra. However, it is to be expected that citrine, for example, owes its lemon-yellow colour to the absorption of blue light and that smoky quartz absorbs wavelengths across the spectrum. At this time, only the clear specimens yield enough light for convincing single-grain 3-D measurements.

Spectra have also been obtained from field samples, originally obtained in the course of luminescence dating programmes. Since, as collected, these are already in the form of grains, it is certain that they originate from many parent crystals and that differing spectra may be expected for individual grains. Some examples of this have been described by Hashimoto *et al.* (1987) who took colour photographs of specimens under continuous x-radiation and showed the both "blue" and "red" grains were observed. Ganzawa *et* al. (2005) have since obtained spectra of one of these samples under the same continuous irradiation conditions.

It has been suggested that the luminescence centres responsible for blue emissions can be converted to centres that emit in the red by annealing to a temperature above 867^{o}C, the transition temperature from beta quartz to tridymite. A corollary is that quartz crystals formed under high temperature (as opposed to hydrothermal) conditions should already emit in the red. Four of our field samples: SK11, SE3/5, MTFQ and GD20, emit mostly in the red and this presumably reflects the conditions of formation of their parent rocks. This aspect of the physics of quartz forms part of our programme that is still to be implemented. However, a pilot experiment on grains from a single crystal, WRQ, in which the sample was heated to 920^{o}C for one hour, did not convert blue emission to red. This will be explored further.

Some Specific Examples

As an illustration, figure 1a shows a spectrum from a single crystal of clear hydrothermal vein quartz (WQQ). It has been given a laboratory radiation dose of 270Gy. It shows emission at 2.6eV (470nm) with a main peak at about 250^{o}C. This emission is common to many quartz samples and the luminescence centre is attributed to aluminium substituting for silicon in the lattice. There is a suggestion of emission at about 300^{o}C and this is also consistent with previous work on quartz (Krbetschek *et al.* 1997).

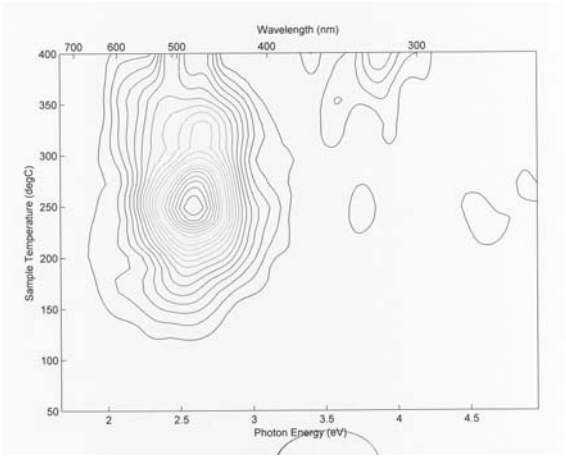

Figure 1 a Sample WQQ 3-D spectrum of 5 mg

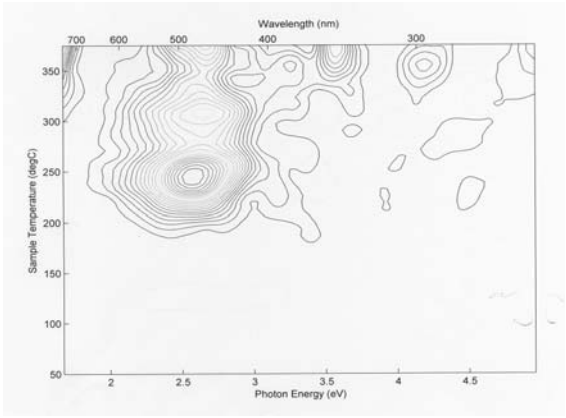

Figure 1b Sample WQQ rum of a single 320 μm grain

The x- and y- scales are the same in both figures but the single grain spectrum stops at 375°C The intensity scales have been adjusted so that the number of contours is the same.

This is a fairly bright sample and single-grain spectra were successfully obtained from it. One of these is shown in figure 1b. It is substantially the same as the "bulk" spectrum and this was true for four individual single grains. Although the intensities varied rather more than would be expected from a nominal 300-350μm range of grain sizes, these results are consistent with the composition of the crystal being uniform. In the present case, the administered laboratory dose was 270Gy which is larger than would normally be found in samples used for luminescence dating. However, the observed intensity indicates that single grain spectra would be obtainable at doses comparable with those found in field samples.

It is common for the luminescence of feldspars to be much brighter than that from quartz and this proved to be so in the present case. Because of their high luminosity, single-grain spectra can be obtained from smaller grains and at smaller administered doses. Examples are given in figures 2a and 2b. Figure 2a shows specimen NSAB from Sacheuga, Zimbabwe, acquired from the British Museum of Natural History and described as "albite Dup A". Albites have high sodium content and the spectrum does indeed show typical characteristics of an albite, with emissions at 280 and 570nm (Prescott and Fox 1993, Krbetschek *et al.* 1997). However, additionally, there is emission at about 420nm which is characteristic of orthoclase, as shown in figure 2b by ORTH18L. This suggests that, even in a single grain, the sample shows distinct albite and orthoclase phases, which is common among feldspars. This spectrum is also unusual in being very bright: the spectrum of figure 2a was obtained with a radiation dose of only 13Gy. Figure 2b is sample ORTH18L, an orthoclase feldspar of high potassium content from Broken Hill. The spectrum is typical of potassium feldspars (Prescott and Fox 1993, Krbetschek *et al.* 1997) with emission at 400nm over a range of temperatures. An unresolved weaker emission at about 500nm is also seen; this is common in potassium feldspars.

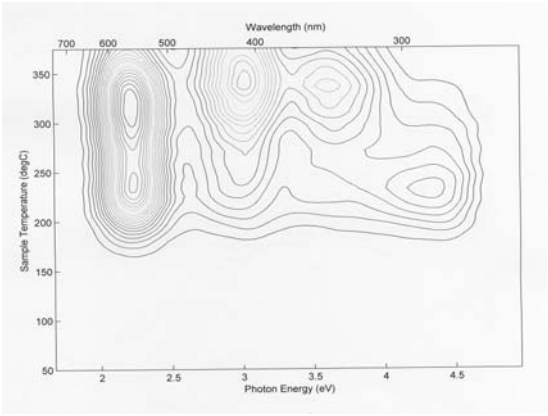

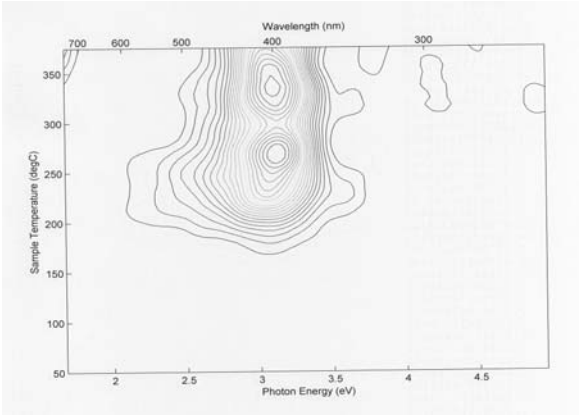

Figure 2a Figure 2b

3-D spectra of a single 320 μm grains of feldspar

2a Sample NSAB Dup A, nominally albite, an aluminosilicate with high sodium content. The presence of emission near 400nm suggests an admixture of orthoclase, c.f. figure 2b.

2b Sample ORTH18L, high-potassium feldspar, characterised by emission near 400nm, 3.1eV.

Acknowledgements

Many aspects of the luminescence dating programme have been supported by AINSE and the present project is supported by AINGRA07124

References

Ganzawa Y., Furukawa H., Hashimoto T., Sanzelle S., Miallier D. & Pilleyre Y. 2005 Single grain dating of volcanic quartz from pyroclastic flows using red TL. Radiation Measurements, 39, 479-487

Hashimoto T., Yokosaka K. & Habuki H. 1987 Emission properties of thermoluminescence from natural quartz—blue and red response to absorbed dose. Nuclear Tracks and Radiation Measurements 13, 57-66

Krbetschek M.R., Götze J., Dietrich A. & Trautman T. 1997 Spectra from minerals relevant to luminescence dating. Radiation Measurements 27, 695-748

Prescott J.R., Fox P.J., Akber R.A., & Jensen H.E. 1988 Thermoluminescence emission spectrometer. Applied Optics 27, 3496-3502

Prescott J.R. & Fox P.J. 1993 Three-dimensional thermoluminescence spectra of feldspars. J. Phys D Applied Physics 26, 2245-2254

Raman measurements of hydrogen ions implanted into silicon

Daniel Pyke [1,2] and Jeffrey McCallum [1]

[1] *School of Physics, University of Melbourne, Victoria, 3010*

[2] *Current address: Department of Electronics Materials Engineering, The Australian National University, Canberra, ACT, 0200.*

Abstract:

Hydrogen implantation into silicon forms the basis of the ion cut process which is one way of producing silicon-on-insulator substrates for advanced electronic devices. In an effort to understand how high-fluence hydrogen implantation leads to the formation of cavities and eventually to layer cleavage and lift-off it is important to be able to identify hydrogen-related defects in the as-implanted and thermally annealed silicon substrates. Some of the common methods used to do this are Fourier transform infrared spectroscopy, multiple internal reflection plates and Positron Beam Doppler Broadening and Raman spectroscopy. In our Raman spectrometry investigation of hydrogen implanted crystalline silicon we have examined the effect of the substrate temperature during implantation on the types of stable hydrogen-related defects that are formed. Substrate temperatures in the range 77 – 298 K during implantation and substrates implanted at low temperature and then annealed in the range 400 – 650K have been examined as part of this study. The evolution of the Raman H-related features with low temperature anneals and in the presence of pre-formed cavity bands will be discussed.

Introduction

Hydrogen's importance to future SOI construction is highlighted in the technique "SmartCut"[5], also called ion slicing. The previous most common method for producing silicon-on-insulator (SOI) wafers was by direct ion implantation (generally oxygen) into the wafer substrate, occasionally accompanied by hydrophilic wafer bonding. However, due to this method being time consuming & requiring dedicated ion beam implantation equipment, a search for alternative methods lead to the conception of SmartCut. This particular method is also trademarked, requiring expensive licences to utilise. It has also led to other regions of the scientific community heading efforts to produce a comparable method without requiring this trademark, and hence cost.

The SmartCut process is displayed schematically in Fig. 1.

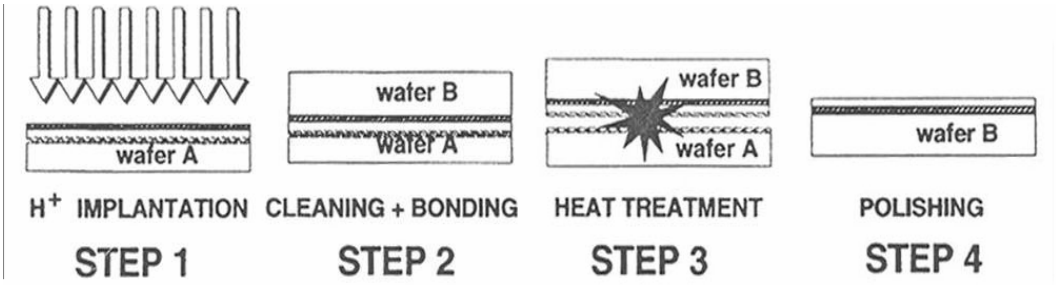

Figure 1 – Diagram of the SmartCut™ process, as detailed by Bruel in his white paper[5].

- Wafer (A) is implanted with a high dosage of hydrogen (~ 1016cm^{-2}), after capping with oxide layer (Step 1).
- Wafer (B) is hydrophilically bonded onto A - becomes the silicon substrate of the SOI device (step 2).

- Undergoes a two tiered temperature treatment: 400-600°C to induce delamination across the H implant, creating a monocrystalline layer atop an oxide cap on a crystal substrate out of wafer B; Higher temperatures (>1000°C) applied to strengthen the chemical bonds (step 3).
- SOI is polished using a number of chemico-mechanical methods (step 4).

Experimental

We implanted p-type B-doped 1-10 Ω.cm <100>-oriented silicon wafers with a dose of 3x1016 ions.cm-2 H+ at a range of energies – 30keV, 100keV - and temperatures of - T=77K or 298K. Additionally, two wafers were implanted with three separate energy implants, at 20, 30 and 40keV and 60, 80 and 100keV, each with the same fluence of 3x1016 ions.cm-2 at T=77K. All samples were mounted at 7° with respect to implantation beam to minimize possible channeling.

Samples from each implantation regime were then exposed to low temperature anneals (T = 150°C – 350°C) in an Argon ambient furnace for 30 minutes.

All samples were analysed with Raman spectroscopy – a technique where the vibrational modes of materials can be studied by their inelastic scattering of light. Generally a coherent source such as a laser is used as the light source. The beam is incident on the material under examination, and the scattered light is spectrally analysed. The fundamental properties of the material can then be extrapolated from the data. This is due to the manner with which the laser light originally interacts with the atoms of the material. The laser light can lose or gain energy relative to the incident beam through interaction with the allowed vibrational modes of the material. This is called a Raman shift: νlaser - νscattered = ΔνRaman

The measured shift can often be used to identify the constituents and structure of the material undergoing study.

The system used was a Renishaw RM1000 UV/Vis confocal micro-Raman spectrometer, with an 1800mm grating, 50µm aperture, 50x Leica objective lens and a 514.5nm Argon ion laser as the excitation source.

Implantation Temperature

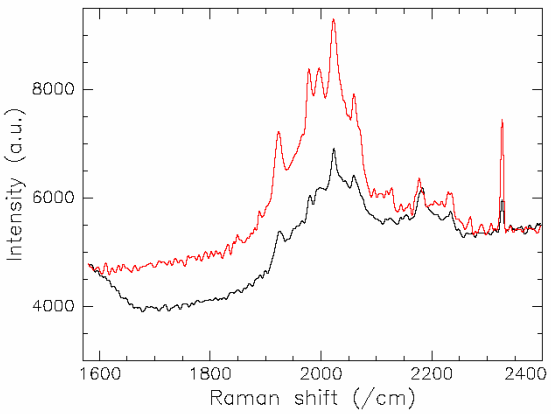

Figure 2- –Raman Spectra from triple H+-implanted Si (dose: 3.1016cm-2, energies: 60keV, 80keV and 100keV) at a) room temperature (T=298K) and b) liquid nitrogen temperature (T=77K).

Most previous studies undertaken dealt with samples implanted at room temperature (T=298K). Our studies examined the influence of substrate temperature during implantation by comparing implants at 77K and at 298K(Liquid Nitrogen temperature). Results show that the range of spectral features is similar for both implants, but higher signal intensity is achieved by liquid nitrogen implants, suggesting that low temperature implantation leads to a higher proportion of the implanted H residing in these Raman-active defects. As we were looking for fine changes in hydrogen signals, T=77K implants were chosen for the remainder of the study.

Thermal Anneal Raman Spectra

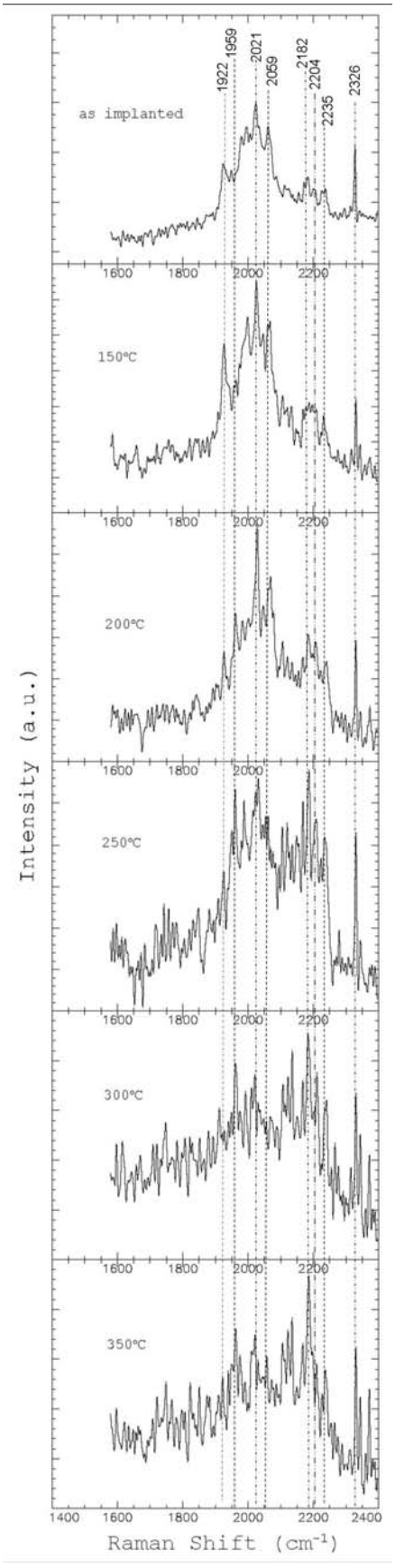

Si-H stretch frequencies – due to bonding within the Si bulk and at the surface – appear within the frequency range from 1900 to 2250cm^{-1} in the as-implanted samples.

There is a large, broad fluorescence peak spread underneath the highest concentration of hydrogen features, from ~1850-2300cm^{-1}.

Line at 2326cm^{-1} has been identified as CO_2 due to surface absorption.

The main H features present in the as-implanted samples (1900-2060cm^{-1}) decrease following the anneals while the initially secondary features (2180-2250cm^{-1}) become the dominant features as temperature increases. Stein reports this as a decrease in the divacancy bands being annealed out.

The feature at 2182cm^{-1} has generally been associated with VH3/V2H6 or SiH4.

The peak at 2235cm^{-1}, along with the whole complex associated with this mode around 2205cm^{-1} has been associated with hydrogen-decorated mono-vacancies (VH4).

Following subsequent anneals, features also evolve in the higher frequency bands above 2300cm^{-1}, noted at 2341cm^{-1} and 2369cm^{-1}. The origin of these features is unknown.

Peaks at 1925, 1957, 2021 and 2059cm^{-1} were reported by Mukashev et.al.[3] immediately after implant, in agreement with these data.

The features at 2185cm^{-1} and 2235cm^{-1} are observed in our as-implanted sample, but Mukashev et.al.[3] only observed them following subsequent (~200°C) anneals of the material.
Hydrogen molecules (H_2) are generally described as located at ~2062cm^{-1} and 2120cm^{-1} – neither of these are notably present in our data, suggesting no gas formation.

Murakami et.al.[1] report a significant hydrogen feature at 2100cm^{-1}, though not significantly apparent in their spectra before T=300°C anneals. This has previously been identified as a monohydride Si-H surface feature on (100) Si by Stein et.al.[2], generally associated with anneal induced H-decorated voids or cavities at the surface.

These features are not seen in our data due to the absence of such voids in our material.

Conclusion

The Implantation at liquid nitrogen temperatures produces more clearly defined features, but in broad agreement with room temperature implants. There is a general degree of agreement with some previous authors over the location of H peaks. The lack of the presence of a feature at $\nu = 2100cm^{-1}$ is in agreement with view that this feature is related to hydrogen decoration of voids or cavities (which are not present in our samples).

Acknowledgements:

Ion implants were performed using the facilities at the Department of Electronic Materials Engineering, The Australian National University.

References

1. K. Murakami, N. Fukata, S. Sasaki, K. Ishioka, M. Kitajima, S. Fujimura, J. Kikuchi & H. Haneda, Phys.Rev.Lett. 77(15), 3161, (1996)
2. H. Stein, S. Myers & D. Follstaedt, J.Appl.Phys. 73 (6), 2755, (1993)
3. B. Mukashev, K. Nussupov & M. Tamendarov, Phys.Lett. 72A (4,5), 381, (1979)
4. W. Dungen, R. Job, Y. Ma, Y. Huang, W. Fahrner, L. Keller, J. Horstmann, Mater.Res.Soc.Symp.Proc., Vol.864, E9.25.1, (2005)
5. M. Bruel, Nucl.Inst.Meth.B., 108:313-19, (1996)

Hydrogen refinement during solid phase epitaxial crystallisation of buried amorphous silicon layers

D.J. Pyke [1,2] and J.C. McCallum [1]

[1] *School of Physics, University of Melbourne, Victoria, 3010*

[2] *Current address: Department of Electronics Materials Engineering, The Australian National University, Canberra, ACT, 0200.*

Abstract

This study concerns the crystallisation of amorphous silicon via solid phase epitaxy (SPE) in the presence of ion implanted hydrogen. Both time resolved optical reflectivity and Rutherford backscattering spectrometry were used to study the crystallisation process. Thermal annealing within the 560°C to 640°C range found an ever decreasing rate of SPE for all concentrations studied (ie C{H}=0.01-0.5at.%). This was further influenced by the location of the implanted hydrogen, with deeper implants having less impact on the crystallisation process. Simulations adequately recreate the refinement process in a perfect amorphous silicon layer, closely matching key elements in the data collected. However, hydrogen is not completely confined to the amorphous layer during crystallisation and it is found to getter to the defect bands that form at the location of the original amorphous/crystalline interfaces.

Introduction:

Solid Phase Epitaxy (SPE) was first described by Mayer et al in 1968[1], which was followed by an in-depth characterisation process at Caltech during the 1970s[2]. SPE is a process where amorphous material rearranges and changes monolayer by monolayer to the crystalline structure of the underlying substrate. Occurring in many semiconductor materials, SPE intrinsically follows an Arrhenius equation details of which have been examined by Olson and Roth[3], though the rate can be retarded or enhanced with particular dopants. Hydrogen in particular is seen to retard the process, with some conflicting reports on what effects varying concentrations cause. The exact mechanism which SPE uses to crystallise is not known, though several molecular dynamics models suggest a number of possibilities[4].

An interesting phenomena noted in SPE of silicon is the refinement of many impurities within the amorphous region. Due to higher solubility within the amorphous phase of silicon, the impurities are segregated and concentrated as the amorphous material is added to the crystalline substrate. In the particular case of hydrogen in surface amorphous layers, research suggested that the segregation retards the SPE process until the hydrogen reaches a critical concentration. At this point, the local concentration of hydrogen exceeds the solubility limit and the excess escapes from the amorphous layer prior to the completion of the SPE provided the free-surface is sufficiently close. However, if the amorphous layer which held the hydrogen is buried within the silicon crystal, the process differs in that it has two amorphous/crystalline (a/c) interfaces refining hydrogen before their paths. The behaviour of the hydrogen in buried layers has not been as well studied as surface layers, and its potential to refine the hydrogen into a narrowly localised profile lends itself to some micro-engineering applications.

At present, the most efficient and economically viable method of producing silicon on insulator (SOI) substrates, upon which to build microelectronic devices, is a process known as ion-cut[5]. Ion-cut uses the implantation of hydrogen ions to high fluence into a silicon wafer and subsequent annealing to induce bond breakage at an

approximate constant depth across the wafer. The hydrogen implanted within the wafer, under thermal annealing, forms bubbles or microcavities within the silicon, damaging the bonds in the crystal. Recent research suggests the point of cleavage may not be the peak ion concentration, but the peak of the damage within the silicon caused by implantation[6]. Independent of the precise location, the implantation is the specific requirement which leads to the wafer slicing. The fluence required to produce cleavage is $\geq 2\times10^{16}cm^{-2}$, a substantial areal density which occupies the bulk of the wafer's production time. If it were possible to reduce the required implantation time, the cost efficiency of the process would increase dramatically in response to small changes.

Utilising the refinement of hydrogen within the amorphous layer prior to high temperature annealing may provide an accelerated ion-cut process. The bubble field range would be decreased, lessening the final roughness of the wafer and necessity for polishing. This work sought to establish how the hydrogen would behave within the amorphous layer during the SPE process prior to the subsequent anneal, attempting to confirm if the segregation occurred within buried amorphous layers similarly to surface layers.

Experimental

The substrate used in this work was a <100> oriented p-type B-doped Czochralski wafers with a resistivity of 5-10 Ω cm. The samples were implanted at T=-10^{o}C with two doses of Si ions: $6x10^{14}cm^{-2}$ at 600keV and $4x10^{15}cm^{-2}$ at 2MeV. Two samples were then implanted at room temperature with 180keV hydrogen ions, at fluences of $5x10^{15}cm^{-2}$ and $1x10^{16}cm^{-2}$ respectively. A third wafer was left intrinsically silicon. All of these ion implantations were performed on a 1.7 MV NEC 5SDH-4 tandem ion implanter at the Department of Electronic Materials Engineering at the Australian National University.

Several techniques were used to characterize the samples before, during and after the SPE process. The location and changes in the amorphous layer were identified with Rutherford backscattering spectroscopy (RBS). In assessing the state of the wafers, a 2MeV $^{4}He^{+}$ analyzing beam was used incident normal to the sample surface, with the detector positioned at a glancing angle of 70^{o} from the normal.

To dynamically monitor the motion of the a/c interface motion during SPE, a time resolved reflectivity (TRR) system measured samples as they were annealed on a resistively heated vacuum chuck stage. The TRR system consisted of a 632.8nm 5mW HeNe laser and an 1152nm 2mW infrared laser. For each laser, interference between laser light scattered from the surface and the buried crystallising interfaces could be used to monitor the interface motion as a function of time.

The evolution of the hydrogen profile was measured using secondary ion mass spectrometry (SIMS). The samples were ion sputtered with a Cs^{+} beam at 250eV and at a relative angle of 58^{o} to the surface. The manufacturer's specified detection sensitivity for hydrogen is approximately 10^{18} atoms.cm^{-3}, a depth resolution of better than 100Å and a precision of within 2%. SIMS analysis was carried out on a Cameca IMS Wf Depth Profiler by Materials Analytical Services, Inc., in Santa Clara, California.

Results

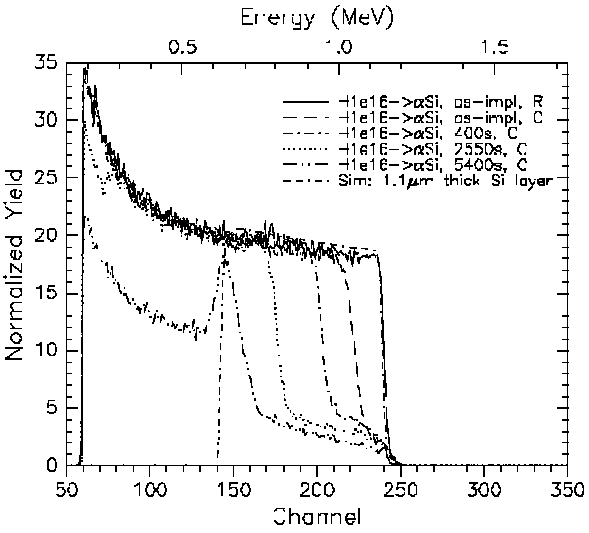

Figure 1- RBS measurements of buried a-Si layer implanted with 180keV Hydrogen annealed at T = 580°C for intervals as labelled. C signifies channelled ions, R signifies random angled ions

RBS in the channelling mode was used to assess the near surface location of the amorphous layer. The higher hydrogen fluence sample was measured initially at both random and channelled angles on a sample lightly annealed at 400°C to planarise the a/c interface, establishing the thickness of the surface crystalline layer. Three different samples annealed at T=580°C were examined, at various stages of SPE – t = 400s, 2550s and 5400s. These data were analysed using the computer code RUMP. A comparison between each of these collections with the lightly annealed samples, listed here as "as-impl", is shown in Fig. 1. Also overlayed on the data is a simulation of a 1.1μm Si layer to illustrate the theoretically calculated centre of the amorphous layer, which seems in good agreement with the collected data. The surface crystal is quite clear between the random and channelled signal, revealing a cap of approximately 250nm above the initial amorphous silicon layer. The rear of the amorphous layer is not initially visible, beyond the depth range of the analysing beam, though enters measurable range after t=2550s. The motion of both a/c interfaces seems distinct, as the rear interface is quite slow relative to the near surface a/c interface in the initial stages of the SPE process. This suggests retardation of the rear interface by the presence of hydrogen within the amorphous layer. SRIM simulations indicated that the hydrogen projected range lay near 1.62μm, within the rear half of the amorphous layer, close to the rear a/c interface. It is interesting to note that the front a/c interface slows down dramatically as it crystallises towards the centre of the amorphous layer. Approximately the same depth is converted within each time interval examined, suggesting that hydrogen was thermally diffusing towards the surface of the layer and impeding the SPE process.

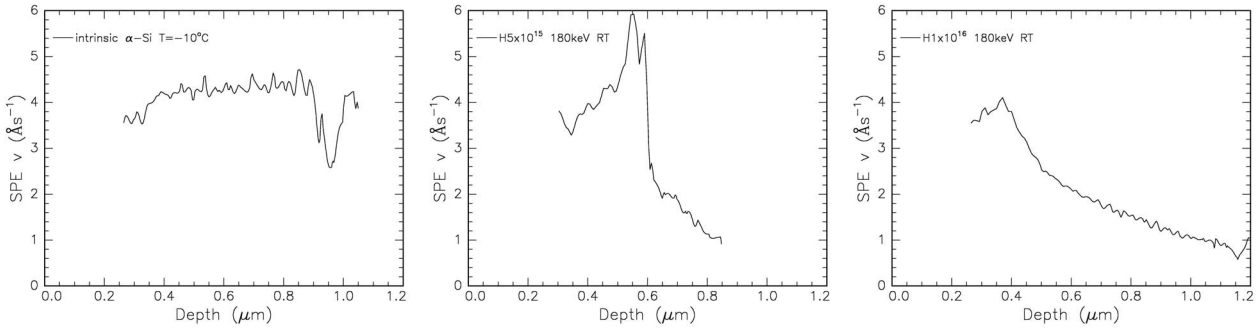

Figure 2- TRR measurements of velocity versus depth.

To establish the rate which SPE was occurring, TRR monitored the samples as they were annealed on a resistively heated stage. The change in reflectivity data collected by the visible 632.8nm laser were used in the computer package GENPLOT to extract the velocity with respect to depth of the a/c interface. For the three samples studied, these traces are shown in Fig. 2. The region measured was the upper half of the amorphous layer as it crystallised, and this seems quite constant in the intrinsic silicon sample, with its relative velocity within 2% agreement with SPE theory. The signals from the two hydrogen implanted samples show a gradual slow down in the SPE rate as the interface moved deeper into the layer. The larger peak in the low dose sample is an abnormality which we believe is merely a software fitting error due to the collapse in the TRR signal in the data collection.

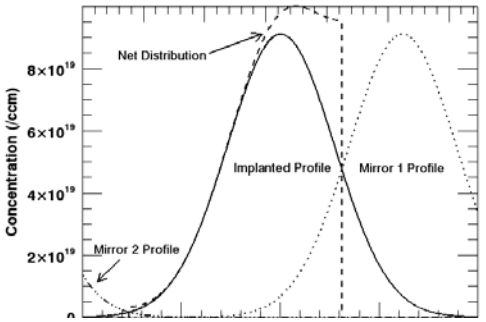

Figure 3 - Schematic of IDL simulations

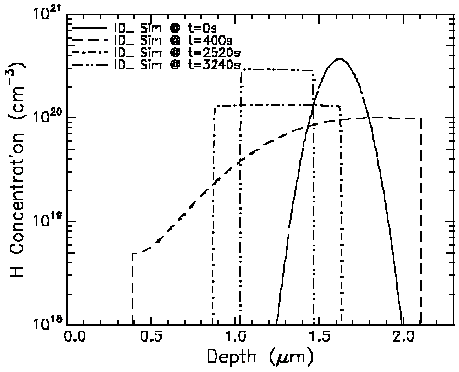

Figure 4 - IDL simulation of H1e16 in buried a-Si layer undergoing SPE.

Prior to the experimentally determining the location of the hydrogen at stages of SPE, the expected crystallisation and refinement behaviour was simulated with the computer code IDL. These simulations used the value of SPE calculated by the intrinsic equation defined by Olson and Roth, modified by a constant to mimic the retardation measured via TRR. Similarly, the hydrogen implantation profile and subsequent diffusion were modelled overlayed with reflection of the hydrogen profiles around the a/c interfaces. The underlying process is shown schematically in Fig 3, while the simulations for the higher hydrogen fluence of $1x10^{16}cm^{-2}$ over the four time intervals studied with RBS are shown in Fig. 4. Note that the last time has been modified from the experimental data, due to the modified intrinsic theory still completing crystallisation prior to t=5400s. When the concentration at the a/c interface is extracted from these simulations, and matched with the velocity data at those times measured experimentally, there is good agreement with previous experimental measurements by Olsen and Roth. These data are shown later in Fig. 6.

In order to ascertain where the hydrogen was present during this crystallisation process, SIMS was used on several samples, twins of those examined by RBS. The spectra from these four samples are shown in Fig. 5. These show a clear skewed Gaussian in the initial hydrogen implant profile, with an integrated areal density of $9.98x10^{15}cm^{-2}$, in excellent agreement with implantation recipe.

The refinement of the hydrogen within the crystallising amorphous layer is in good agreement with that predicted by the IDL simulations, suggesting that despite the assumptions made in the IDL code it is still a useful prediction tool. The unexpected result is the trapping of hydrogen at depths of 145nm and 2.15μm, suggesting defect

bands located at the near surface and EOR a/c interface. Despite the silicon being crystal between the hydrogen source and these defect points at the later stages of the anneal t=2550s and 5400s, hydrogen is still reaching the traps. The trapping efficiency is found to decrease with time suggesting that trap sites may be reaching saturation.

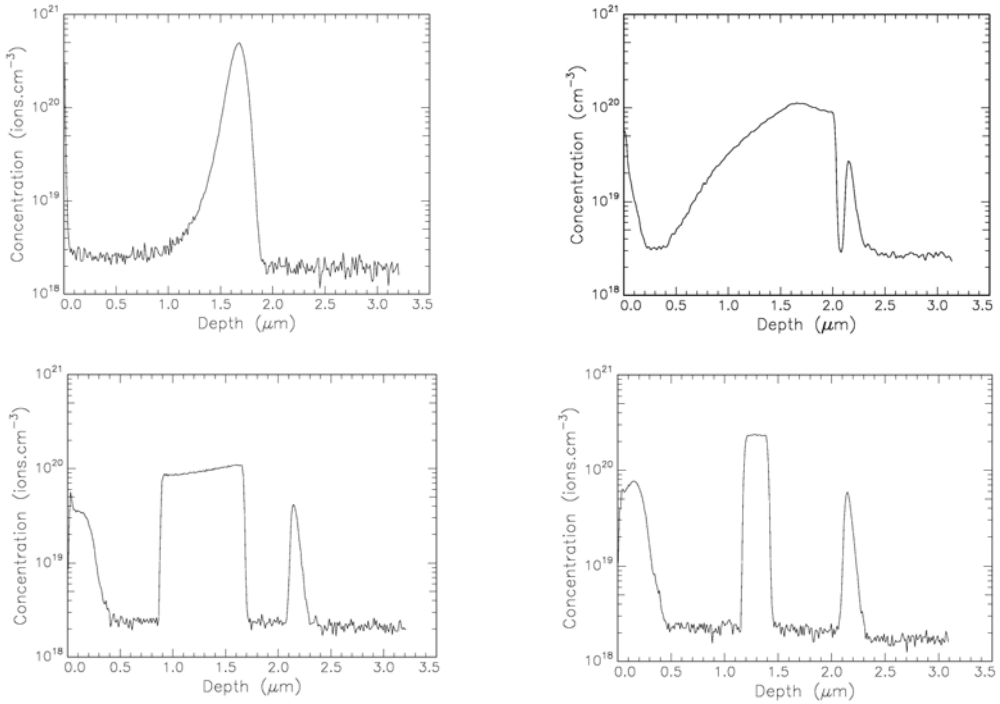

Figure 3- SIMS data (clockwise from top left) t=0,400,2550,5400s

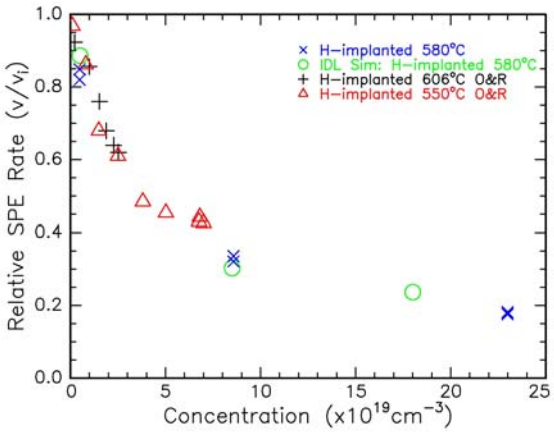

Figure 4- Dependence of SPE rate on H concentration, contrasting with [3]

When the values of the concentration at the front a/c interface are matched with the TRR-measured SPE velocity values, we again find good agreement with previous work by Olson and Roth. This study successfully extends the SPE relationship with hydrogen to five times the previous concentration limit. This is shown in Fig. 6. As mentioned earlier, this figure also overlays the IDL simulation data, again illustrating good agreement with both previous and new results.

Conclusion

Hydrogen was seen to be refined by the SPE crystallising amorphous silicon layers. However, while the bulk was maintained within the amorphous boundaries, hydrogen was trapped at the defect bands associated with the front and rear initial a/c interfaces. The behaviour of SPE in buried amorphous layers was successfully modelled by IDL,

and the range of experimental data extended by five. Due to the lower final concentration and loss of hydrogen from the buried layer, this method is unlikely to improve upon the ion-cut method.

Acknowledgements:

Ion implants were performed using the facilities at the Department of Electronic Materials Engineering, The Australian National University.

References

[1] J.W. Mayer, L. Eriksson, S.T. Picraux and J.A. Davies, *Can. J. Phys*., 45, 1968.

[2] L. Csepregi, E.F. Kennedy, T.J. Gallagher, J.W. Mayer and T.W. Sigmon, *J. Appl.Phys.*, 48, 1977.

[3] G.L. Olson, J.A. Roth, Handbook of Crystal Growth 3: Thin Films and Epitaxy, Part A:Basic Techniques, chapter 7: Solid Phase Epitaxy, pages 255–312. Hughes Research Laboratories, 1994.

[4] J.W. Mayer and S.S. Lau. Electronic Materials Science: For Integrated Circuits in Si and GaAs. Macmillian Publishing Company, 1990.

[5] G.K. Celler & Sorin Cristoleveanu, *J. Appl. Phys.*, 93 (9):4955, 2003.

[6] M. Nastasi, T. Hochbauer, R.D. Verda, A. Misra, J-K. Lee, J.W. Mayer, S.S. Lau, *Nucl. Inst. Meth. B*, 219-220:604, 2004.

Application of environmental isotopes to study aquifer interactions and their impact on groundwater salinisation in western Victoria

M. Raiber & J.A. Webb
Department of Environmental Sciences, La Trobe University, Bundoora, VIC, 3086, Australia

G. E. Jacobsen, R. Chisari, A. A. Williams & B. Neklapilova
Institute for Environmental Research, Australian Nuclear Science and Technology Organisation, Menai, NSW 2234, Australia

A series of environmental isotopes (e.g. radiocarbon, tritium and $^{87}Sr/^{86}Sr$) were used to study aquifer interactions and the origins of groundwater salinisation in western Victoria. Groundwater quality within the aquifer systems (a surficial basalt aquifer and a deep lead aquifer extending over more than 2500km^2) is very variable, ranging from high quality suitable for human consumption to saline brines. The application of stable and radioactive isotopes proved to be a valuable tool to understand the hydraulic connections between these two aquifers, showing that the aquifers are separated over much of the area. However, in close proximity to eruption points, both aquifers are preferentially recharged through volcanic cones and rocky outcrops of highly fractured basalts, resulting in modern (recharged less than 50 yrs. BP) good quality groundwater in both aquifers in these areas.

Investigation of monolithic Si ΔE-E telescope using IBIC and application for radiobiological efficiency estimation in proton therapy

A.B.Rosenfeld [1], A.Wroe [1], A.L.Ziebell [1], D.Prokopovich [1,2], M. Reinhard [3], I. Cornelius [1], R. Siegele [2], D.Cohen [2], A.Fazzi [3], A.Pola [3], S.Agosteo [3], V. Varoli 3, R.Schulte 4

[1] *Centre for Medical Radiation Physics, University of Wollongong, Australia*
[2] *ANSTO*
[3] *Politecnico di Milano, Italy*
[4] *Loma Linda University Medical Centre, USA*

Abstract

This work proposes the use of a unique ΔE-E telescope to measure and quantify hadron fields used in therapeutic applications. The device has been tested using both modulated and un-modulated therapeutic protons with good result.

Introduction

Hadron therapy has many advantages when compared to conventional x-ray therapy through precise delivery of radiation doses to the target volume and a reduction in the dose to normal tissues surrounding the target. This advantage is the direct result of how charged hadrons deposit a large portion of energy at the end of their track in a high dose region known as the Bragg peak. Heavy ions also exhibit a high LET and in combination with secondary charged particles generated through interactions of the primary therapeutic beam can result in a net increase in the Radiobiological Efficiency (RBE). It is important to consider such variations as they may have a direct effect on the outcome of treatment.

Materials and Methods

Silicon detector instrumentation has found an interesting application in radiation therapy for Quality Assurance (QA) in treatment delivery. Avalanche silicon photodiodes originally designed for positron emission tomography (PET) studies have been adapted for use in dose verification for heavy ion therapy [1]. SOI based microdosimetry [2] developed at the CMRP has been implemented in proton and neutron therapies for GEANT4 Monte Carlo verification and radiobiological dosimetry. Silicon strip detectors have also been used for beam profile monitoring along the Bragg Peak [3].

In this study we are presenting a new approach to dosimetry in ion therapy based on primary and secondary particles identification in real time during ion therapy delivery. Identification of primary and secondary particles at any point of the phantom is important for Monte Carlo simulation verification and prediction of the radiobiological effect. This approach is based on a miniature ΔE-E Si telescope (Figure 1) with an in-built 2 μm ΔE-detector and 500μm E–detector [4]. ΔE-E technique for charged particle identification is well known in experimental nuclear physics but has never been previously applied to radiation therapy. The charge collection of this device was recently investigated in detail using IBICC techniques [5]. The advantage of this device is in a small cross sectional area (1mm^2) that makes it suitable for high fluence applications with minimal pile-up.

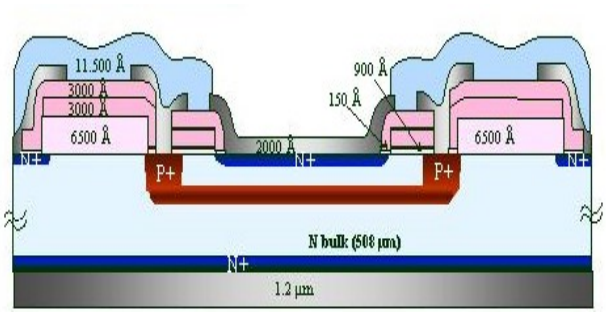

Figure 3: Schematic of the ΔE-E Si telescope (fabricated by ST Microelectronics, Italy).

The noise level of both thee and ΔE stage was 8keV. Portable readout electronics for coincidence acquisition of the ΔE-E stages was developed at the Politecnico di Milano. Calibration of the system was completed using alpha particles from Am-241 source. Experiments were carried out at Loma Linda proton therapy facility for various positions along a 100MeV Bragg Peak (BP) and Spread Out Bragg Peak (SOBP). The ΔE-E detector was placed at different depths on the central axis within a homogeneous polystyrene phantom with the sensitive area closely attached to the polystyrene allowing for the collection and registration of secondary particles. The depth dose profile for both the modulated and un-modulated proton beam was established using a Markus ionization chamber. During the course of the experiment the dose rate to the detector was monitored and remained at 0.25cGy/spill with a stable profile of approximately 5cm diameter.

Results and Discussion

Figure 2 shows absorbed dose distribution for an un-modulated 100MeV proton beam in the polystyrene phantom with associated ΔE-E telescope measurement positions.

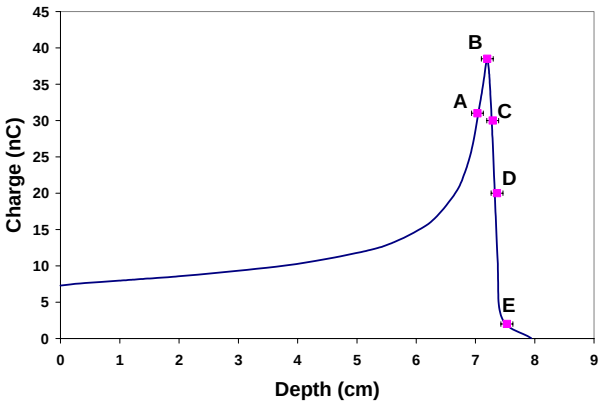

Figure 4: Bragg Peak for 100MeV measured by Markus chamber in a polystyrene phantom with corresponding ΔE-E telescope measurement positions (A-E).

Figure 3 displays the experimentally measured 2D ΔE-E coincidence spectra obtained at points A and E for consideration and discussion. This data clearly demonstrates the ability of this device to measure the primary proton beam and secondary scattered particles generated by both the primary beam and fast neutrons.

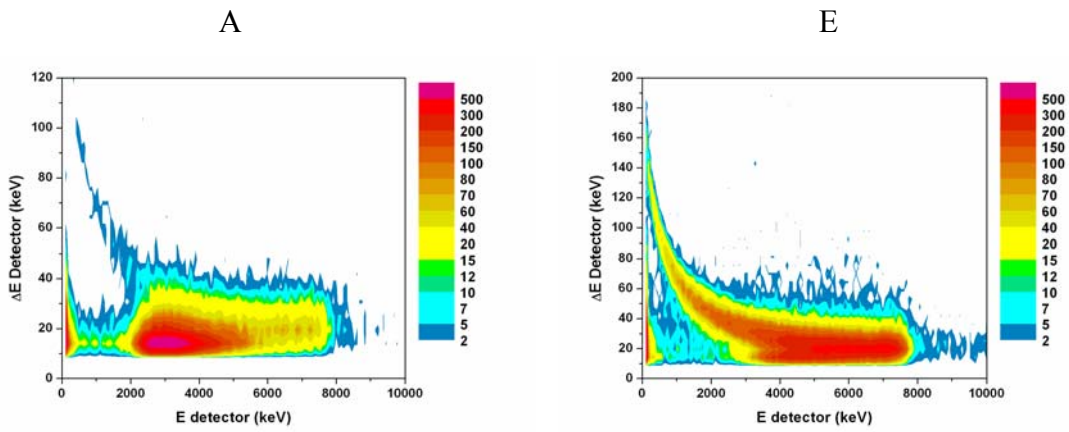

Figure 5: ΔE-E coincidence plot measured in polystyrene for the un-modulated 100MeV proton beam for measurement points A and E.

As the depth increases the energy of the primary proton beam decreases which is reflected in the ΔE-E plot. Extension of the proton locus above kink in the spectra (8MeV energy deposition within the E detector) occurs where protons fully deposit maximum energy in E-stage of Si telescope. For higher energies of incident protons (200-250MeV typically used in the treatment of deep seated tumors) it is expected that inelastic nuclear products such as alpha particles will be observed and can be accounted for in biological effect calculations.

This method of radiation detection for ion therapy in addition to silicon microdosimetry provides an ideal tool for verification of Monte Carlo simulations that are increasingly used for dose planning. Identification of the charged particles is an additional benchmark in MC verification compared to 1-dimensional microdosimetric spectra. This technique also allows for contribution from the primary beam (highest statistics on ΔE-E plot) and associated neutron field, produced through primary beam interaction with beam modification devices, to be simultaneously measured and compared.

Using 3D ΔE_i-E_j plot of events i, j it is possible to prescribe a radiobiological weight $Q_{i,j}$ for each point based on existing radiobiological models. From this it is possible to determine the average RBE of the radiation field given the following relationship:

$$RBE = \sum_{i.j} \frac{N_{i,j} Q_{i,j}}{N}$$

Where, $N_{i,j}$ is a statistics of i,j event on the matrix and N total number of events on a ΔE-E plot.

Conclusions

The proposed technique and instrumentation allows for a new approach to dosimetry in ion therapy. This technique has been successfully tested with both a modulated and un-modulated proton beam at various positions along the BP and SOBP. Further developments of this technology will allow for direct correlation of ΔE-E telescope signal to RBE.

References

1 Kapusta, M et al. The LSO/APD array as a possible detector for in-beam PET in hadron therapy, IEEE Trans. Nucl. Sci., 51, 1389-1394, 2004

2 A.Wroe, et al. “Silicon Microdosimetry in Heterogeneous Materials: Simulation & Experiment”, IEEE Trans on Nucl. Sci, NS-53, 3738-3744, 2006

3 V.P. Cosgrove et al. Microdosimetric Studies on the Orsay Proton Synchrocyclotron at 73 and 200MeV, Rda.Prot. Dosim., 70:493-496,1997

4 A. Fazzi, S. Agosteo, A. Pola, V. Varoli, P. Zotto, A Micrometric Thickness Silicon Diode Proposed as a Microdosimeter, IEEE Trans. Nucl. Sci. Vol. 53, N. 1, Feb.2006, pp. 312-316

5 I. Cornelius, et al. “Charge collection imaging of a monolithic telescope for radiation protection” , *Radiat .Protec. Dosim*., Dec 2006, Vol 122, (1-4), pp. 387-389

Gold nano-structures electroplated on au electrodes of quartz crystal microbalance (QCM) for enhanced mercury vapour sensitivity

Y M Sabri, D K Sood, S K Bhargava and S J Ippolito
Industrial Chemistry Group, School of Applied Sciences,
RMIT University, Melbourne, Victoria 3001, Australia

Abstract

Mercury vapour exhausted from industrial refineries poses many environmental and health related risks. Therefore it is becoming more crucial to develop cheap, stable and robust sensors to sense atmospheric mercury concentration in areas polluted by industrial gaseous effluent. The ability of gold to absorb and amalgamate mercury is the basis of many commercially available mercury vapour sensors. In particular it is highly desirable to enhance the dynamic stability and mass sensitivity of Quartz crystal microbalance (QCM) based sensor for the continuous operation in industrial environments. In this work, we have improved the mass sensitivity of a QCM by increasing the surface area of the electrodes by electroplating gold nanostructures on them. Approximately two times larger response magnitude (frequency change) towards Hg than non-modified QCM based sensors was achieved. Electroplating was conducted for different times, varying from 5 to 60 seconds. The morphology of the plated structures was studied with a scanning electron microscope (SEM). Intricate porous nanostructures with feature dimensions of 50 to 250nm were observed. Secondary Ion Mass Spectroscopy (SIMS)* was utilised to study the depth profiles of amalgamated Hg on the Au thin films.

1. Introduction

Quartz crystal microbalance (QCM) is thought to be a desirable means for monitoring the elemental mercury gas [1] due to its unique combination of mechanical, electrical, chemical and thermal properties, which has led to its commercial significance [2]. By analytically solving the one dimensional equation of motion, Sauerbrey showed that for an ideal layer of foreign mass deposited on the surface of a QCM the frequency change (Δf) proportional to the deposited mass Δm can be calculated:

$$\Delta f = -\frac{2 f_0^2}{A\sqrt{c_{66}\rho_q}}\Delta m = -S_f \Delta m \qquad (1)\ .$$

Where S_f represents the integral mass sensitivity or Sauerbrey constant and is proportional to the square of the fundamental frequency, f_0, inversely proportional to the surface area, A, and increases proportionally with the overtone number [2]. C_{66} and ρ_q are the quartz properties.

Gold is well known as a passive collector of mercury, which then can be released by heating and measured by spectroscopic techniques [3]. It is well known that the surface-to-volume ratio (SVR) has great influence on the properties of a sensor. In resent years, one dimensional (1D) nanostructures, such as gold nanowires have attracted much attention since the SVR has great influence on the material performance [4,5]. When applying QCM as a sensor, it is important to obtain high sensitivity towards the analyte of interest. One way of achieving this has been to increase the surface area of the electrodes, thereby allowing a higher number of analyte molecules per unit area, resulting in a larger response magnitude [6]. Attempts employing soft dextran hydrogels as a means of surface enlargement have been made,

however have not substantially improved the binding capacity of the surface [7,8]. Furthermore, a soft interface causes a dissipation of energy and results in dampening of the shear wave [9], thereby reducing the sensitivity of the crystal. By introducing a rigid porous gold layer using electroplating, we show how the QCM Au electrode surface area can be enlarged, thereby avoiding the dissipation effect obtained by soft gels like polymer templates.

2. Gold Electrode Preparation

The electro-deposition was performed using a two-electrode system in a solution containing 2.718g/L hydrogen tetrachloroaurate (III) hydrate and 0.177g/L lead(IV) acetate (from Sigma-Aldrich, Australia). A potential of –2V was applied between the two electrodes of the crystal (Cathode) and Au foil (anode). This ensured that Au nano-structures were formed on both Au electrodes of the QCM. A non-modified crystal served as a control, while three others were set aside for surface modification by electrochemical deposition. A Phillips XL30 Secondary electron microscope (SEM) was used to characterize the electrode surface of each sample. The micrographs, with different electro-deposition times, are shown in Figure 1.

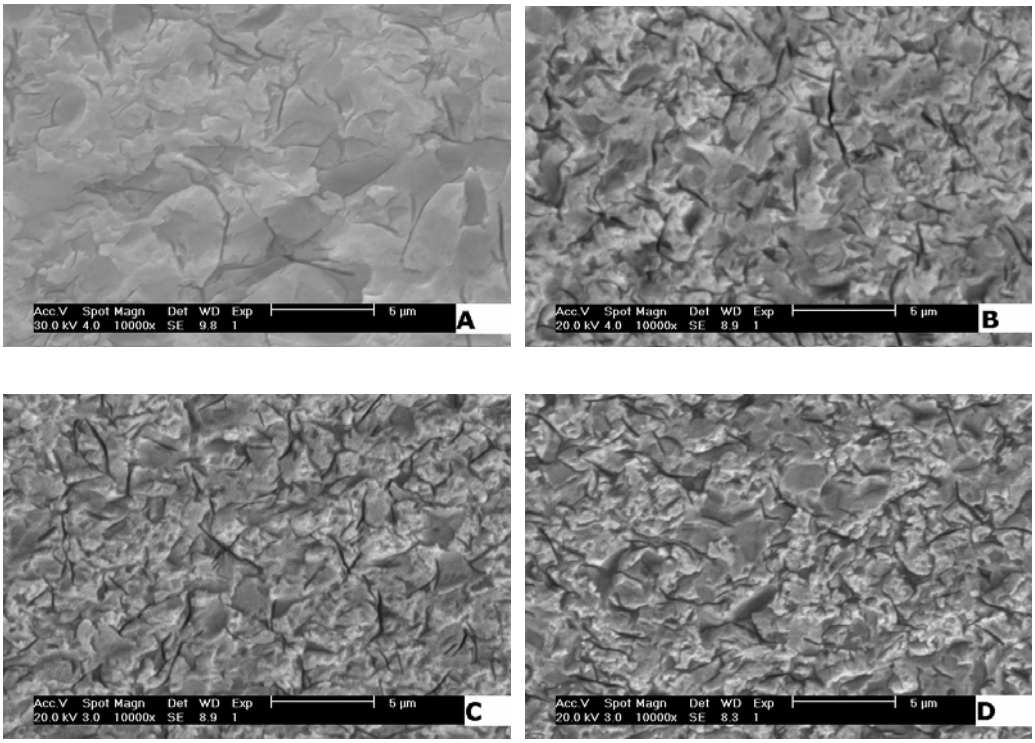

Figure 1: SEM image of non-modified and electro-deposited Au electrodes (A) Non-modified surface, (B) 10s electro-deposited, (C) 40s electro-deposited and (D) 50s electro-deposited time.

The images suggest that with continuing electro-deposition of Au onto the evaporated Au electrodes, an increasingly rougher surface is achieved. The images show larger and deeper ‘cracks’ with increasing electro-deposition time. Intricate porous nanostructures with feature dimensions of 50 to 250nm were observed. Therefore a higher surface area of Au would be exposed.

3. Experimental Procedure and Results

Two QCMs were used as the frequency determining element in an oscillator circuit, where the oscillation frequency was measured by an Agilent 53131A frequency counter. Similarly, the resonant frequency of two other QCMs was measured by a commercial phase lock loop system, RQCM 603902. A constant gas flow rate of 200sccm was provided by a specially developed 4 channel mass flow controller system, while data acquisition was performed via a conventional desktop computer. A Hg concentration of 4.31mg/m^3 was obtained by heating permeation tubes (P/N 137-100-0030-S56-C90) to 70ºC. The Hg concentration was calibrated using $KMnO_4$ (Sigma Aldrich, Australia.) trapping method and analysed by ICPMS (Inductively coupled plasma mass spectroscopy). Different chamber temperatures were obtained by changing the voltage input to halogen bulbs located near the QCM sensors. The crystals were tested at operating temperatures of 34, 42, 58 and 76ºC.

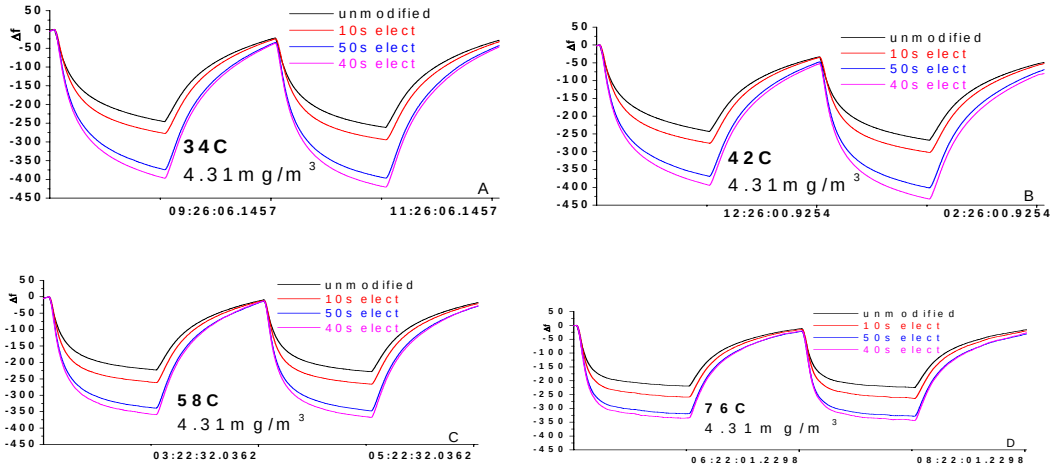

Figure 2: Sensor responses for different electrodeposited surfaces exposed to Hg at (A) 34ºC, (B) 42ºC, (C) 58ºC, (D) 76ºC.

The dynamic response of each QCM sensor is shown in Figure 2. The repeatability of the sensors was confirmed by repeating each pulse twice at the different operating temperatures. This was done by exposing the sensors to 4.31 mg/m^3 of Hg for one hour and dry nitrogen for the next hour before repeating the same process again. The responses of the modified sensors were always higher than that of the non-modified QCM. This was true for all tested operating temperatures. It was also observed that the response for the 40 and 50s electro-deposition QCMs was nearly twice that of non-modified at the lower operating temperatures of 34ºC and that the 40s sample had the largest response magnitude for all tested operating temperatures.

By analysing the curves in Figure 2, it can be observed that the regeneration of all the sensors is remarkably consistent with the non-modified QCM. (i.e. the responses all return back to the baseline frequency, Δf=0Hz). Interestingly, the increased response during absorption period of the modified QCMs indicates that they have adsorbed/amalgamated more Hg than the non-modified surfaces and yet, the regeneration rate is high enough that they return to the same baseline as the non-modified QCM within the same 1 hour period. It has been suggested by Nowakowski et al. [10] that the structure of Au/Hg amalgam is not stable and changes with time. Therefore, it is necessary that the sensor be exposed to Hg for only a short period of time and have a large response magnitude. Based on this, it can be concluded that

electro-deposition technique satisfies both these criteria. Furthermore, Nowakowski et al. also suggested that local defects on the thin gold film surfaces play a fundamental role in the rate of amalgamation. Therefore, we hypothesise that electro deposition technique may not produce large defect points on the surface and may to some extent just purely increase surface to volume ratio, explaining the increased regeneration behaviour observed for modified (electroplated) surfaces.

Each of the electrode surfaces were analysed using SIMS depth profiling. The results in Figure 3A and 3B show that the 10s electro-deposited sample has a different adsorption/amalgamation behaviour than the other sensors. As expected, the non-modified Au surface contains the least Hg. One should realise that these surfaces have been characterized by SIMS two months after the sensing process was performed. Surprisingly, SIMS characterisation revealed that the 10s electro-deposited Au surface contained the most Hg within this group of sensors, indicating that the other surfaces favoured adsorption behaviour towards Hg rather than forming an amalgam. These results therefore indicate that the 10s electro-deposited sample may have contained more point defects and so encouraged amalgamation rather than adsorption alone. It should be noted that this behaviour is not desirable for regenerable sensors for use with elemental Hg vapour sensing application.

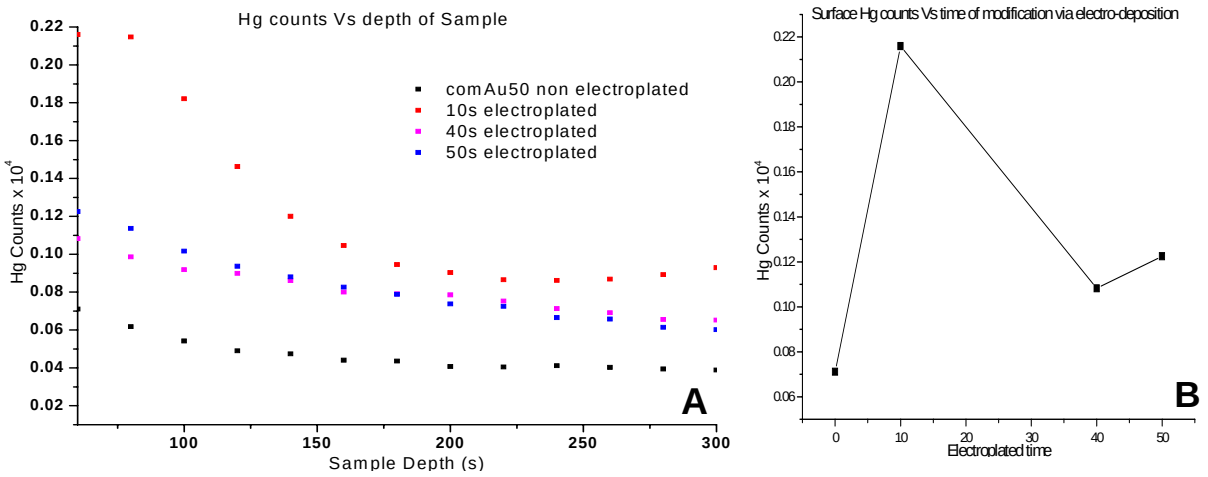

Figure 3: SIMS depth profile. (A) Hg count with respect to sample depth for all four Au electrode surfaces and (B) Hg count at the surface for non-modified and modified samples.

Conclusion

The mass sensitivity of gold electrode QCM sensors for mercury vapour has been shown to be substantially increased by electroplating gold nanostructures on them. Using SEM and SIMS to analyse the adsorption/amalgamation behaviour of Au-Hg confirmed that modification of Au surface via electro-deposition increased the affinity of Au for Hg. Results show that different modification parameters change the behaviour of Au towards Hg. That is, it was observed that a 10s electrodeposited Au had similar adsorption/regeneration behaviour as 40 and 50s electro-deposited surfaces. However SIMS revealed the presence of a higher Hg content on this surface after two months, thus suggesting that the 10s sample contained more point defects and so encouraged amalgamation rather than adsorption. Therefore it can be concluded that further work needs to be conducted in order to repeat and confirm this phenomena. Once done, the information from this work can be used to develop a

more safe, simple and economic method for continual monitoring of mercury vapour in industrial refinery gaseous effluents.

Acknowledgements

The Authors would like to acknowledge the support from the Australian Institute of Nuclear Science and Engineering (AINSE) for SIMS at ANSTO under an AINSE grant no AINGRA06164P. We would also like to thank Dr James Tardio, Mr. Armand Atanacio and Dr. Kathryn Prince for their help.

References

1. L. Spassov, D.Y. Yankov, A.N. Mogilevski and A.D. Mayorov. Rev. Sci. Instrum. 64, 1993, 225
2. C. Steinem et al. Angew. Chem. Int. Ed. 2000,39, 4004–4032.
3. C. Battistoni, E. Bemporad, Applied Surface Science, 103, 1996, 107–111.
4. X. Wang, J. Zhang, Z. Zhu, J. Zhu, Colloids and Surface A: Physicochem. Eng. Aspects 276, 2006, 59–64.
5. S. Keebaugh, A. K. Kalkan, W. J. Nam, S. J. Fonash, Electrochemical and Solid-State Letters, 9, 2006, H88–H91.
6. D. V. Noort, R. Rani, Mikrochim. Acta.136, 2001, 49–53.
7. J. Rickert, A. Brecht, W. GoÈpel, Biosens. Bioelectron. 12, 1997, 567.
8. S. Storri, T. Santoni, M. Minummi, M. Mascini, Biosens. Bioelectron, 13, 1998, 347.
9. F. Hook, M. Rodahl, P. Brzezinski, B. Kasemo, Langmuir, 14, 1998, 734.
10. R. Nowakowski, T. Kobiela, Z. Worfram, R. Dus, Applied Surface Science, 115, 1997, 217–231.

Localisation of trace metals in hyper-accumulating plants using μ-PIXE

R. Siegele [a], A.G. Kachenko [b], Y.D. Wang [c], M. Ionescu [a],
N.P. Bhatia [a] and D.D. Cohen [a]

[a] *Australian Nuclear Science and Technology Organisation (ANSTO), PMB1, Menai, NSW 2234, Australia*

[b] *Faculty of Agriculture, Food and Natural Resources, The University of Sydney, NSW 2006, Australia*

[c] *School of Botany, The University of Melbourne, VIC 3010, Australia*

Abstract

PIXE is a very sensitive technique to simultaneously measure a wide range of elements with high sensitivity and map their distribution using a focused ion beam. We demonstrate high resolution mapping of metals in plant leafs at 5μm resolution and its application mapping metal distribution in metal-accumulating plant tissues. The importance of sample preparation is discussed by direct comparison of freeze-substitution and freeze-drying techniques.

Keywords: localization, metal hyperaccumulation, nuclear microprobe, PIXE.

Introduction

PIXE is a powerful analytical technique used in many research areas. Combined with a microbeam it becomes a powerful tool to map the distribution of elements across a specimen.

At ANSTO we have used μ-PIXE extensively to map trace elements in plant and animal tissues. More recently we have applied μ-PIXE to study the localisation of trace metals in metal indicator and hyperaccumulating plant species. A plant is said to be a metal hyper-accumulator if it concentrates trace metals above a minimum threshold concentration in above ground tissues. This threshold varies according to the metal involved [1-2]. In contrast, metal uptake in indicator plants to aboveground tissues is relatively unregulated, thus internal concentrations are a passive reflection of external levels [3].

To understand the mechanisms that allow these metal-accumulating plants to tolerate high concentrations of normally toxic metals, the spatial localisation of the metal accumulation has to be known. In this study we demonstrate cellular and sub cellular localisation of trace metals in plant tissues with μ-PIXE using freeze-drying and freeze-substitution sample preparation techniques.

Experimental

Plant samples were analysed using the ANSTO High Energy Heavy Ion Microprobe (HIMP) [4]. The samples were analysed using a 3MeV proton beam with a typical spot size of between 3 and 5μm. At this spot size beam currents between 0.1 and 0.5 nA can be achieved, which is sufficient for PIXE analyses.

A high purity Ge detector was used with a 100mm^2 active area, located 33mm from the sample. A 100μm Mylar foil was used to reduce low energy X-rays and thus pile-up in the μ-PIXE spectrum. This setup allowed the detection of the accumulated trace metals such as Ni and Cu with high sensitivity.

Sample Preparation AND Results

In the microanalysis of biological tissues sample preparation is one of the most important steps, which is also the case for µ-PIXE. Plant samples need to be dried and thin sectioned for µ-PIXE analysis. In the case of plant material exposed to metals it has to be ensured that this process does not result in the redistribution of the metal and that the cell ultrastructure is preserved. Because of the high spatial resolution of µ-PIXE even small movements have to be avoided.

In previous experiments, we have employed a simple technique that involved the hand sectioning of the samples followed immediately by snap freezing of the sections in liquid nitrogen. The sections were subsequently freeze dried [5]. However, with this technique at the best sections of 50µm can be achieved. This limits the lateral resolution in µ-PIXE, because of the possible overlap of the distribution of a particular element from different sample depth. As a result cellular resolution is difficult to achieve because overlapping cell layers are mapped in this case.

In order to prepare thinner (<50µm) sections we employed a freeze-substitution technique using dry tetrahydrofuran (THF) as a solvent. Pålsgård et al. [6] described this technique and found it suitable for biological sample preparation. Using this sample preparation technique, sections of ca. 10µm or thinner can be prepared with a microtome.

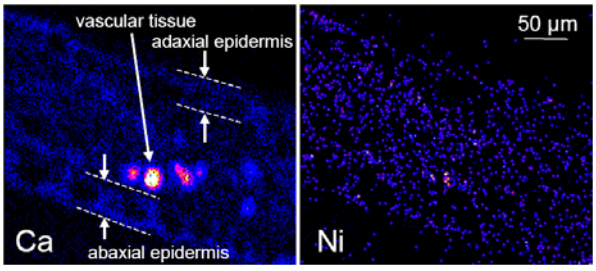

Figure 1. Elemental maps for Ca (left) and Ni (right) of the Hybanthus floribundus subsp. floribundus leaf section prepared by freeze substitution in THF

A leaf section of Ni-hyperaccumulating *Hybanthus floribundus* subsp. *floribundus* was prepared by this technique and analysed with µ-PIXE. Elemental maps shown in Figure 1 were extracted using GeoPIXE [7]. The Ca concentration map demonstrates that in the epidermis layer cellular resolution can be achieved and that the Ca is concentrated in the cell walls. However, in the central region of the leaf, individual cells can not be resolved because the cells in this region are much smaller and a number of cell layers overlap. This can also be seen in the optical micrograph (not presented) where the cell structure is not visible in this part of the leaf.

In contrast K showed a homogeneous distribution across the analysed section (not presented), with the average K concentration across the section much lower than the K concentration measured by ICP-AES. The K concentration from ICP-AES was 2.0% DW, while the average concentration across the leaf calculated from µ-PIXE was 0.4% DW. Similarly, the Ni concentration was much lower in freeze-substituted sections (0.1%) than measured using ICP-AES (0.8%) DW. These results suggest that some of the K and Ni were washed out of the sample during the freeze-substitution process.

These findings are consistent with recently published results by D. Budka et al. [8] who found a substantial loss of Ni in Ni-hyperaccumulating *Berkheya coddii* prepared by this technique. The authors reported Ni loss of up to 90% in leaf samples treated with THF. Like Ni, K is considered a readily mobile element and in our study freeze-

substitution with THF resulted in significantly lower K concentrations than ICP-AES results.

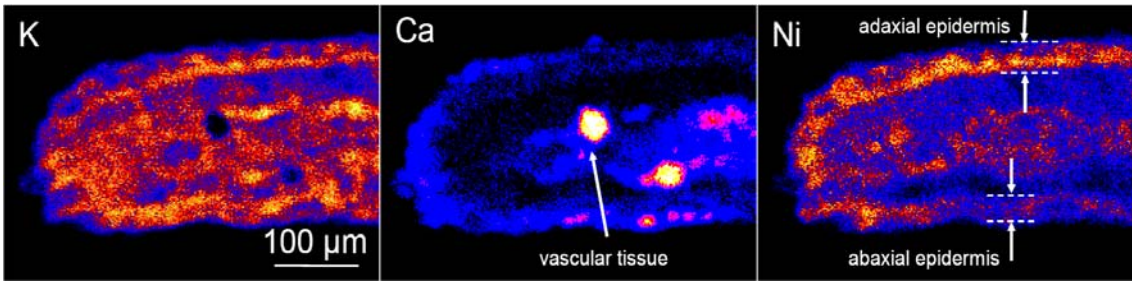

Figure **2.** Elemental maps of K (left), Ca (centre) and Ni (right) taken on a hand sectioned cryo-fixed freeze-dried *Hybanthus floribundus* subsp. *floribundus* leaf.

The Ni image showed some indication of the cell structure in the epidermal layers with Ni enriched in the cell walls. However, the Ni concentration was too low to quantify the distribution pattern.

To compare these results a set of samples were hand sectioned, cryo-fixed and freeze-dried following the procedure described by Bhatia et al. [5]. Figure 2 shows elemental maps from the samples prepared in this way.

These maps clearly showed a variable distribution of metals across the leaf section. Notably, across all three maps, the adaxial and abaxial epidermis was clearly defined. Moreover, in the K and Ca maps the cell walls were visible in the epidermis, although not with the same clarity as in Figure 1. The Ni map also suggested enrichment of Ni in the cell walls.

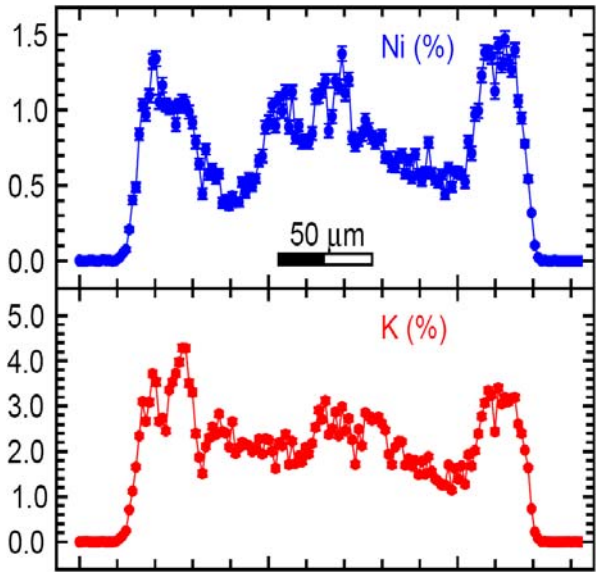

Figure 3. Quantitative elemental profiles of Ni and K across the freeze-dried leaf section shown in Fig. 2

However, compared with the images of the freeze-substituted sample, the Ni image of the freeze-dried sample clearly illustrated the anatomical structure and corresponding localization pattern. In particular Ni concentrations were highest in the adaxial and abaxial epidermal layers, but also in the vascular bundles that dominate the central region of the leaf.

The K map showed a similar distribution with high K concentrations in the epidermal layers of the leaf surface. In addition, it showed a second layer with high K concentration, that was likely vascular bundles.

The Ca map showed that the Ca is concentrated in the epidermal cell walls, however, this is less apparent, because of the overlap of a number of layers smearing out the image. Furthermore, the Ca concentration in the vascular bundles was approximately 5-10 fold higher than in the epidermal tissues.

Quantitative elemental profiles for Ni and K (Figure 3) taken across the central region of the freeze-dried section clearly showed the higher concentration of both elements

in the epidermal tissues and vascular bundles supporting the results of the elemental maps in Figure 2.

Conclusions

We have demonstrated that μ-PIXE can be used to localise the areas of metal accumulation in leaf tissues.

The simultaneous mapping of various elements can be used to explore the physiological mechanisms that allow these plants to accumulate and in some cases hyperaccumulate metals.

In sections prepared using freeze-substitution (THF), we showed that cellular and to a lesser extent sub-cellular resolution can be achieved. However, this procedure resulted in the loss of metals and possible redistribution. Conversely freeze-dried leaf sections preserved cellular metal concentrations, however only cellular resolution was achieved.

Acknowledgments

The authors thank Kevin Ansary for his help in running the accelerator and the Tandem Accelerator Operations Team for their efforts. A.G. Kachenko, B. Singh, Y.D. Wang and A.M.J. Baker acknowledge funding by grants from the Australian Institute of Nuclear Science and Engineering (AINSE). A.G. Kachenko acknowledges the financial assistance provided by the Australian Government through an Australian Postgraduate Award scholarship.

References

1. A.J.M. Baker, S.P. McGrath, R.D.Reeves and J.A.C. Smith, "Metal Hyperaccumulator Plants: A Review of the Ecology and Physiology of a Biological Resource for Phytoremediation of Metal-Polluted Soils," in *Phytoremediation of Contaminated Soil and Water,* edited by N. Terry and G. Bañuelos, Boca Raton, FL, USA: CRC Press Inc, 2000, pp. 85-107.
2. A.J.M. Baker,R.R. Brooks, *Biorecovery* **1** (1989) 81-126.
3. A.J.M. Baker, *J. Plant. Nutr.* **3** (1981) 643-654
4. R. Siegele, D.D. Cohen, N. Dytlewski, *Nucl. Instr. and Meth.* **B158** (1999) *31-38.*
5. N.P. Bhatia, K.B. Walsh, I. Orlic, R. Siegele, N. Ashwath, A.J.M. Baker. *Fun. Plant Biol.* **31** (2004) 1061-1074.
6. E. Pålsgård, U. Lindh, G.M. Roomans, Microsc. *Res. Tech.* **28** (1994) 254-258.
7. C.G Ryan, *Nucl. Instr. and Meth.* **B181** (2001) 170–179.
8. D. Budka, J. Mesjasz-Przybyłowicz, G. Tylko, W.J. Przybyłowicz, *Nucl. Instr. and Meth.* **B231** (2005) 338-344.
9. R. R. Brooks, *Plant Soil* **48** (1977) 541-544.

Wafer scale etching of lithium niobate using conventional diffusion process

Vijay Sivan, Lam Bui, Anthony Holland, Suresh Bhargava and Arnan Mitchell
RMIT University, GPO 2476V, Melbourne, VIC 3001

Timothy Priest
Defence Science Technology Organisation, PO Box 1500, Edinburgh, SA 5111, Australia

A novel method for wafer scale texturing of lithium niobate is presented. The surface texturing is achieved by etching a bare Lithium niobate substrate using the conventional Ti diffusion process at high temperature. Material properties of the etched sample are analysed using x-ray diffraction (XRD), X-ray photoelectron spectroscopy (XPS), energy dispersive spectroscopy (EDS) and Fourier Transform Infra-red (FTIR) spectroscopy methods.

Establishment of efficiency function for the gamma-ray spectrometry system

Michael Smith
Australian Nuclear Science and Technology Organisation

Gamma-ray spectrometry system is widely used for the quantification of radioactive components of material. The quality of gamma-ray spectrometry measurement depends directly on the accuracy of detection efficiency for a particular geometry set-up.

This presentation demonstrates the methodology and procedure of obtaining precise gamma-ray detection efficiency. The presentation gives details in dead-time corrections due to incapability of accepting a further pulse while the system processing a pulse, pile-up effect due to the limited time resolution of an amplifier and coincidence-summing corrections due to two or more photons emitted in sequence within the resolving time of the spectrometer.

A TEM study of Si-SiO_2 interfaces in silicon nanodevices

Paul Spizzirri [1], Sergey Rubinov [2], Eric Gauja [3], Laurens Willems van Beveren [3]
Rolf Brenner [3] and Steven Prawer [1]

[1] *Centre of Excellence for Quantum Computer Technology, School of Physics, University of Melbourne, Melbourne, Victoria, 3010.*

[2] *The Bio21 Molecular Science and Biotechnology Institute, University of Melbourne, Melbourne, Victoria, 3010.*

[3] *Centre of Excellence for Quantum Computer Technology, School of Physics, University of New South Wales, Sydney, New South Wales, 2052.*

Abstract

The fabrication of micro- and nano-scale silicon electronic devices requires precision lithography and controlled processing to ensure that the electronic properties of the device are optimized. Importantly, the Si–SiO_2 interface plays a crucial role in defining these properties. While transmission electron microscopy (TEM) can be used to observe the device architecture, substrate / contact crystallinity and interfacial roughness, the preparation and isolation of the device active area is problematic. In this work, we describe the use of focussed ion beam technologies to isolate and *trench-cut* targeted device structures for subsequent TEM analysis. Architectures studied include radio frequency, single electron transistors and electrically detected, magnetic resonance devices that have also undergone ion implantation, rapid thermal and forming gas anneals.

Introduction

Current trends in semiconductor device fabrication have seen the realisation of sub-100nm lithographic processing in silicon. While many of the processing steps involved are now considered routine, there are implications for smaller device geometries and their interactions with neighboring atoms/interfaces. This is most evident in systems where the active elements comprise only a few atoms and where interfaces like that of Si-SiO_2, play a significant role in the operation of the device (e.g. MOS).

Work is being undertaken in this laboratory to develop a solid state quantum computer (QC) which is particularly sensitive to its electronic environment including that of the device substrate. Using shallow donor placement strategies, phosphorus ions are located within tens of nanometers from the substrate surface which is functionalized with MOS circuitry. The resulting number of processing steps that such a device undergoes before measurement can be significant and the underlying structures fabricated are very small (i.e. < 1 micron).

The importance of having analytical techniques capable of reporting on the structure/function of nano-electronic devices cannot be overstated, however finding those that will allow the fabrication pathway to remain intact for study is problematic. While state-of-the-art electron microscopic tools are well suited to the task of device analysis, it has been the development of focused ion beam (FIB) technologies that has solved the problem of sample isolation/preparation for analysis. In this work, we describe the use of electron and focused ion beam techniques for the identification and isolation of solid state structures for high resolution TEM analysis. Areas of interest for this analysis include: measurement of the gate oxide thickness after processing, observation of interfacial roughness and defects or damage to the silicon caused by processing.

Experimental Details

Devices were fabricated using conventional photo- and electron-beam lithographic techniques to create MOS structures on silicon. Oxide layers (field and device) were thermally grown in a triple wall quartz furnace and aluminium contacts were electron beam deposited. A ~100nm gold protective layer was sputter deposited onto the sample prior to ion beam processing to protect underlying structures. Electron beam imaging, which allowed identification of the area of interest and focused ion beam milling were both performed on an FEI NOVA dual beam FIB/SEM. The gallium LMIS of the FIB was also used to pattern a protective platinum layer onto the area being prepared for *liftout*. This is necessary to protect surface structures (i.e. sample integrity) from the gallium beam which can mill away structures as well as being implanted resulting in amorphised near surface regions. Once the membrane was removed, samples were positioned atop a carbon membrane and imaged using an FEI TECNAI TF20 TEM.

Sample Preparation

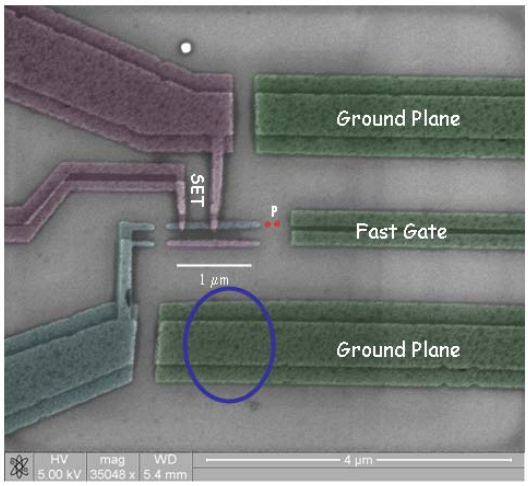

Figure 1. False coloured SEM image of the RF-SET device imaged prior to liftout. The area to be analysed is circled (blue).

One example of a device that underwent FIB preparation and TEM analysis is the radio frequency, single electron transistor (RF-SET) shown in Figure 1. This device has a number of aluminium contacts patterned onto a high quality (device) Si-SiO_2 surface. Two red dots are depicted to indicate the location of the two phosphorus donors which were implanted. The area circled (blue) encompasses a ground plane which is the area of interest for the ensuing TEM analysis.

Shown in Figure 2 is a lower magnification SEM image of the same device following Au coating and Pt deposition which defines the liftout region. The field oxide and device oxide areas are also depicted for clarity along with the photolithographic wirebond contacts (i.e. gold coloured). Figure 3 shows the finished membrane ready for removal and analysis using the TEM.

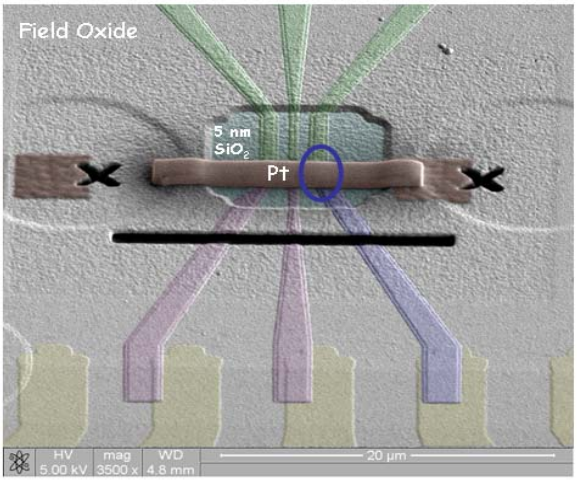

Figure 2. False coloured SEM image of the gold coated RF-SET with the protective Pt coated area imaged prior to membrane milling. The area of interest is circled (blue).

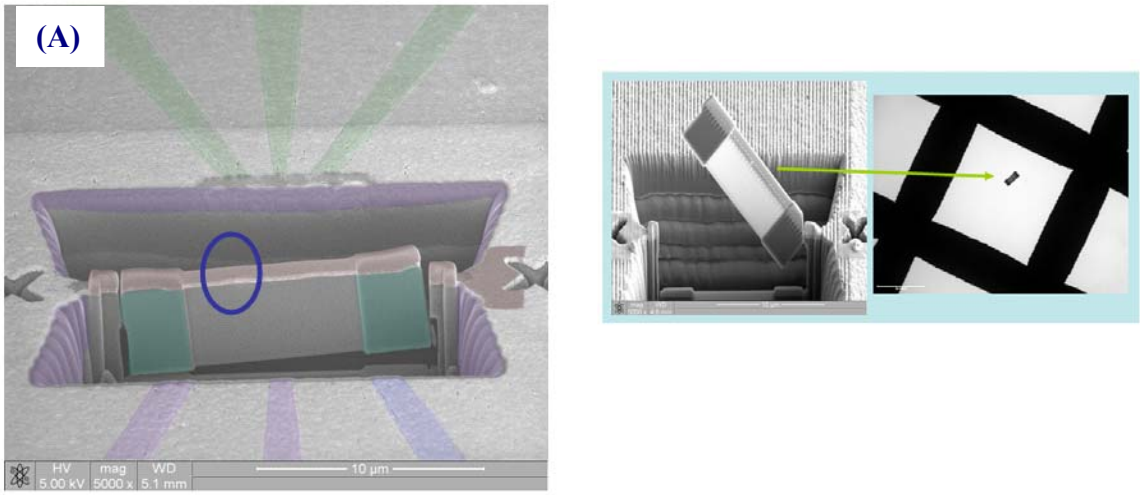

Figure 3. False coloured SEM images of (A) the liftout region (membrane) following FIB milling and (B) a membrane undergoing transfer for TEM analysis. The analysis area of interest is circled in (A) (blue).

Interface Analysis Using TEM

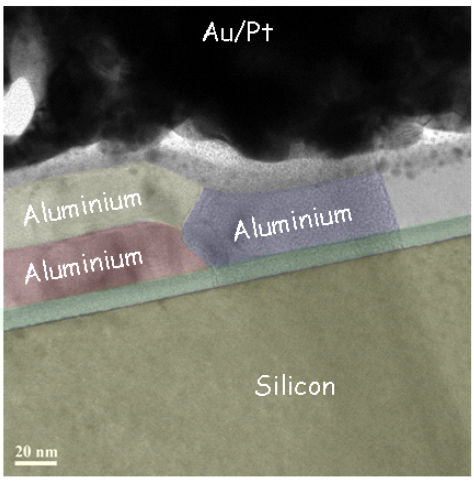

Figure 3. False coloured, medium resolution TEM image of the Si-SiO_2 interface with aluminium contacts.

Interface analysis was performed to characterize the: SiO_2 layer, Si-SiO_2 interface, aluminium schottky contacts and underlying silicon for dislocations or damage arising from processing. Shown in Figure 3 is a cross sectional view of the Si – SiO_2 – Al_2O_3 - Al interfaces. The aluminium grains (crystal), which have an interfacial oxide, are evident in the image as is the insulating SiO_2 layer. The Au and Pt overlayers provide contrast in the regions above the device surface.

Depicted in Figure 4 is a higher resolution image of the same region where it is clear that all of the interfaces are sharp and well defined suggesting that there is good process control. Secondly, the high quality device oxide, which is supposed to be ~5nm thick, is actually ~8.5nm thick. This difference in thickness is significant and has implications for the successful implantation and activation of dopant ions when using low ion energies. Finally, it is worth noting that there are no defects evident in the underlying silicon.

The quality of the Si-SiO_2 interface was also examined and compared to areas where field oxides (~200nm thick) had previously been grown and etched back with a high quality thermal oxide (5nm) subsequently regrown. This is standard practice in low noise MOS device fabrication, used to reduce leakage currents. Shown in Figure 5 is one area of a high quality SiO_2 layer which is ~5nm thick and exhibits a sharp interface. In comparison, the image shown in Figure 6 shows a less sharp Si-SiO_2 interface which has also undergone field oxide etchback and device oxide regrowth. For this sample, there is some evidence of interfacial roughening (< 1nm). This type

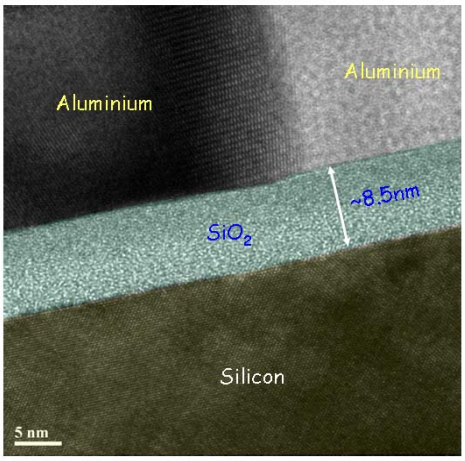

Figure 4. False coloured, high resolution TEM image of the Si-SiO_2-Al interfaces.

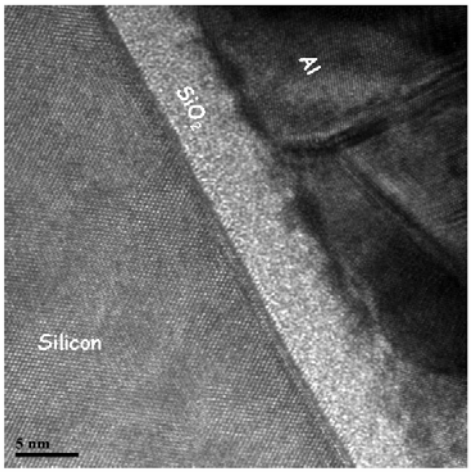

Figure 5. High resolution TEM image of an Si-SiO_2 interface with aluminium contacts.

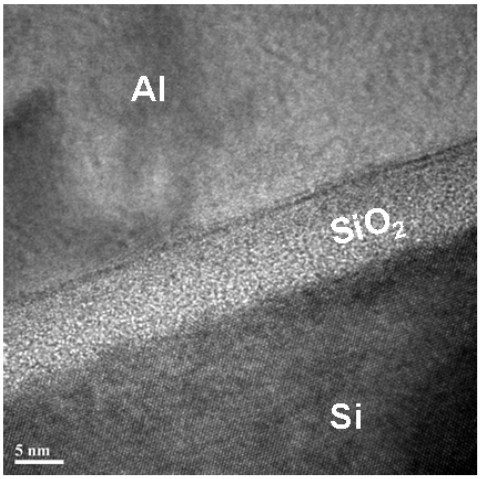

Figure 6. High resolution TEM image of a Si-SiO_2-Al interface that has undergone field oxide etchback and thermal oxide regrowth with some evidence of interfacial roughening.

of interface may result in a reduced performance for MOS devices so it is important to understand the mechanisms by which these interfaces are formed.

Conclusions

FIB prepared TEM samples were used in this work to study the resulting architecture of nano-scale structures used for quantum measurement. They were dissected with sub-micron precision from larger areas and issues surrounding the final silicon dioxide thickness were easily identified. Some interfacial roughening was also observed and may be associated with field oxide etchback and thermal oxide regrowth processes. This effect is still being investigated. These techniques ultimately confirmed the final device architecture and provided information which can be used to feedback into the fabrication process to optimize device geometries.

Acknowledgements

The work is funded by the Australian Research Council, the Australian Government and US Army Research Office under Contract No. W911NF-04-1-0290.